Nanoscale

The Core Contribution of Transmission Electron Microscopy to Functional Nanomaterials Engineering

Journal:	*Nanoscale*
Manuscript ID	NR-FEA-08-2015-005460.R1
Article Type:	Feature Article
Date Submitted by the Author:	02-Nov-2015

Complete List of Authors:	Carenco, Sophie; College de France, UPMC, CNRS, Laboratoire de Chimie de la matière condensée de Paris; moldovan, Simona; Institut de Physique et Chimie des Matériaux de Strasbourg (IPCMS), UMR 7504 du CNRS Roiban, Lucian; Université de Lyon, Insa-Lyon, Mateis Florea, Ileana; Laboratoire de Physique des Interfaces et des Couches Minces, Portehault, David; Laboratoire Chimie de la Matière Condensée de Paris, UPMC Univ Paris 06, CNRS UMR 7574 Valle, Karine; CEA-Le Ripault, DMAT-Laboratoire Sol-gel et Simulation Belleville, Philippe; CEA, DAM, LE RIPAULT, Boissière, Cédric; Laboratoire de Chimie de la Matière Condensée de Paris, Collège de France ROZES, Laurence; Université Pierre et Marie Curie, Chimie de la Matière Condensée de Paris Mezailles, Nicolas; CNRS, Université Paul Sabatier, Drillon, Marc; Institut de Physique et Chimie des Matériaux de Strasbourg (IPCMS), UMR 7504 du CNRS Sanchez, Clement; Laboratoire Chimie de la Matière Condensée de Paris, UPMC Univ Paris 06, CNRS UMR 7574 Ersen, Ovidiu; IPCMS, DSI

The Core Contribution of Transmission Electron Microscopy to Functional Nanomaterials Engineering

Sophie Carenco,[1] Simona Moldovan,[2] Lucian Roiban,[2,5] Ileana Florea,[2,6] David Portehault,[1] Karine Vallé,[3] Philippe Belleville,[3] Cédric Boissière,[1] Laurence Rozes,[1] Nicolas Mézailles,[4] Marc Drillon,[2] Clément Sanchez,[1] Ovidiu Ersen[2]**

[1] Sorbonne Universités, UPMC Univ Paris 06, CNRS, Collège de France, Laboratoire de Chimie de la Matière Condensée de Paris, 11 place Marcelin Berthelot, 75005 Paris, France

[2] Institut de Physique et Chimie des Matériaux de Strasbourg (IPCMS), UMR 7504 CNRS-Université de Strasbourg (UdS), 23 rue du Loess, 67037 Cedex 08 Strasbourg, France

[3] CEA, DAM, Le Ripault, F-37260 Monts, France.

[4] Laboratoire Hétérochimie Fondamentale et Appliquée, Université Paul Sabatier, UMR CNRS 5069, 118, route de Narbonne, 31062 Toulouse Cedex 9, France.

[5] Current address: Université de Lyon, INSA-Lyon, Matériaux : Ingénierie et Science (Mateis), 7 Avenue Jean Capelle, 69621 Villeurbannne, France

[6] Current address: Laboratoire de Physique des Interfaces et Couches Minces (LPICM), UMR 7647 CNRS-Ecole Polytechnique, Route de Saclay, 91128, Palaiseau Cedex, France.

E-mail: ersen@ipcms.unistra.fr; clement.sanchez@college-de-france.fr

Abstract: Research on nanomaterials and nanostructured materials is burgeoning because their numerous and versatile applications can contribute to solve societal needs in the domain of medicine, energy, environment, STICs. Optimizing their properties requires in-depth analysis of their structural, morphological and chemical features at the nanoscale. In a transmission electron microscope (TEM), combining tomography capabilities with electron energy loss spectroscopy and high-resolution imaging in high-angle annular dark-field mode provides access to all these features on the same object. Today TEM experiments in three dimensions are paramount to solve difficult structural problems associated with nanoscale matter. This approach allowed a thorough morphological description of silica fibers as well as a quantitative analysis of the mesoporous network of binary metal oxide prepared by template-assisted spray-drying and the analysis of the degree of homogeneity of amino functionalized metal-organic frameworks. Besides, assessing the morphology and internal structure of metal phosphide nanoparticles was a milestone in understanding phase segregation phenomena at the nanoscale. By extrapolating to larger classes of materials, from soft matter to hard metals and/or ceramics, this approach allows probing small volumes and uncovering materials characteristics and properties at two or three dimensions. Altogether, this feature article aims at providing (nano)materials scientists with a representative set of examples that illustrates the capabilities of modern TEM and tomography that can be transposed to their own research.

Keywords: electron microscopy; HR-TEM; STEM-HAADF; EELS; 3D-TEM; electron tomography; nanomaterials; nanoparticles.

1. Introduction

1.1 Complexity of nanomaterials:

Nanosciences, as biology, is one of the key fields that are contributing to a high level of scientific and technological developments of this 21st century.[1–7] Nanomaterials and related systems are already strongly impacting the domains of energy (fuel cells, batteries, thermoelectric devices, photovoltaic and photoelectrochemical cells…) environment (catalysis, photocatalysis, sensors, smart membranes, functional and protective coatings…), information technologies (micro-optics and photonic devices, microelectronics, smart display devices…) and health (biomaterials, biosensors and biomicrofluidic devices, therapeutic carriers for theranostic, cosmetics…).[7–15],[16] The development of these scientific domains is intimately associated with the ability and creativity of chemists to rationally design and synthesize original nanomaterials and/or nanostructured materials. Nanomaterials derived from bottom-up routes are versatile and offer a wide range of possibilities for tailoring innovative architectures in terms of chemical and physical properties, and shaping. Moreover, nanoparticles are key nanobuilding blocks to design nanocomposites that facilitate integration, miniaturisation and multifunctionalisation of the devices. Today, many nanomaterials synthesized through bottom-up approaches allow the tailoring of properties from the atomic to the mesoscopic length scales.[17–25]

This feature article aims at providing materials scientists with selected examples of structural and chemical questions that were solved by using TEM along with analytical and tomographic capabilities. Because it allows precise analysis of nanoscaled morphological features, transmission electron microscopy (TEM) was soon recognized as an essential characterization tool in the field of nanoparticles (NPs) synthesis, and, over the last 30 years, it contributed extensively to the burst of nanomaterials and nanostructured materials.[7],[26–28],[29],[30] Today, nanosciences span a wide range of compositions,[31] including alloys,[32,33] multicationic oxides,[34,35] polyanionics species, chalcogenides,[36–40] borides, phosphides,[41] phosphates, fluorides,[42] carbon nanotubes,[43] graphene derivatives[44] and organic compounds such as micelles, liposomes, polymers,[45] block-copolymer-based micelles[46] and latexes.[47] Moreover, new or optimal properties are very often due to controlled

morphology (core-shell, nanorattles, nanomatches, dumbbells, octopodes, stars, janus, nanotubes, zeolites, mesoporous materials…),[31],[48],[49] nano-heterogeneity (composition gradients, defects, anionic or cationic gaps) or nano-porosity. Such an innovative field of research will mature through the developments of systematic studies of phase diagrams or composition diagrams at the nanoscale.[50] In all cases, by using the appropriate analysis mode, TEM is the authoritative characterization tool. Indeed, an extraordinary amount of research based on TEM has appeared in the field of nanomaterials, indicating the wide interest of chemists, physicists and materials researchers for nanosciences. This vast research field is illustrated by several key reviews and feature articles.[29,51–55]

The nanoparticles diversity is depicted in Figure 1 through few selected examples. 2D TEM micrographs of nanoscaled objects (metals, metal oxides), and nanoporous materials (carbon) are gathered on the top of the figure. Complex shapes such as gold nanostars (A)[56] or metal chalcogenide octapods (F)[57] are better understood with a 3D model. Heterostructures such as core-shell nanoparticles (B),[58] binary nanorods (C),[59] ternary nanowires (E)[60] and core-shell nano-pyramids (H)[61] furthermore require to locate the elements inside their structure. Porosity also contributes to the nanostructure and should be appropriately identified and quantified, such as for mesostructured carbons (D)[62] and bimetallic oxides (G).[55]

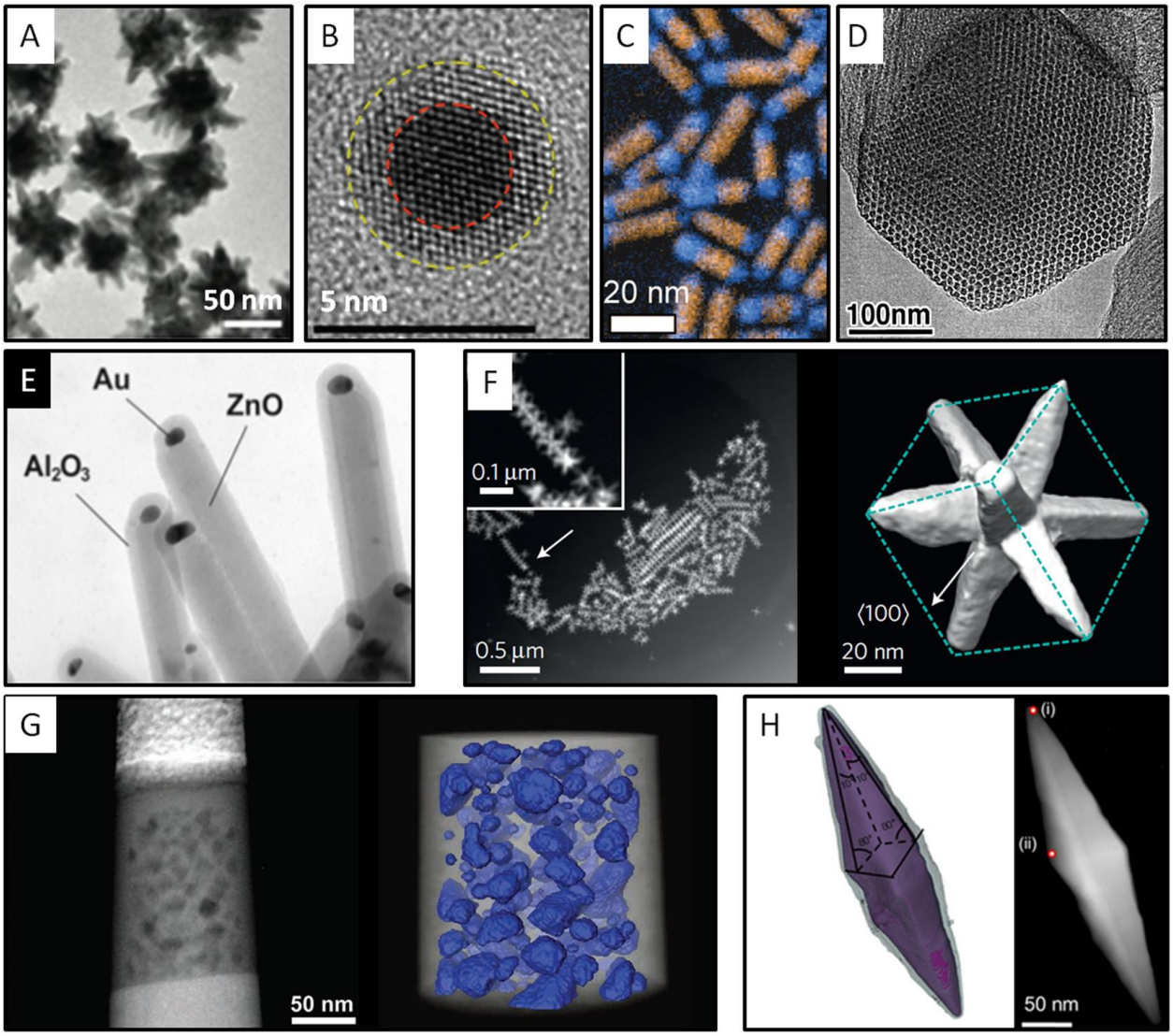

Figure 1: (A-E) Examples of 2D TEM micrographs of complex 3D objects. (F-H) TEM micrographs and 3D reconstructions. (A) Gold nanostars.[56] (B) Core-shell Au@Ag nanoparticle.[58] (C) CdS-Cu_2S binary nanorods.[59] (D) Nanoscaled mesoporous carbon.[62] (E) Al_2O_3@ZnO nanowires that encapsulate a gold nanoparticle.[60] (F) CdS-CdSe octapods.[57] (G) Needle-shaped pilar from a porous layer of $La_2Zr_2O_7$.[55] (H) Core-shell gold-silver nanopyramid.[61]

This nano-menagerie was constructed *via* numerous chemical strategies among them: hydrolytic[2,3],[63] and non hydrolytic condensations,[64–66] polymerization by coordination,[67–71] redox assisted condensation, redox assisted nucleation, galvanic displacement of metals,[72,73] phosphidation of metal nanoparticles, sulfidation, boridation, exfoliation of lamellar compounds into nano-slabs,[74–76]

lego-like nanochemistry…[77,78] New approaches developed during the last ten years emphasize the crucial impact of the heating and the excitation modes (conventional heating, microwave heating, ultrasounds, magnetic, light stimuli…) and of the reaction media (water, organic solvents, ionic liquids, molten salts…) on the shape, size and accessible compositions of the synthesized nanoparticles.[79] In terms of morphological control at the mesoscale, templated growth and/or oriented attachment processes can yield the formation of original architectures such as mesocrystals,[20] hierarchically structured porous materials.[19] For these latter, the use of 3D TEM to allow a better understanding of the structure and construction mechanism is mandatory.[54]

Figure 2 illustrates some nanomaterials and nano-objects developed in our research groups together with the chemical strategies and processes used to optimize their formation. The chemical and processing pathways are represented by a cartoon and the resulting nanomaterials by TEM pictures.

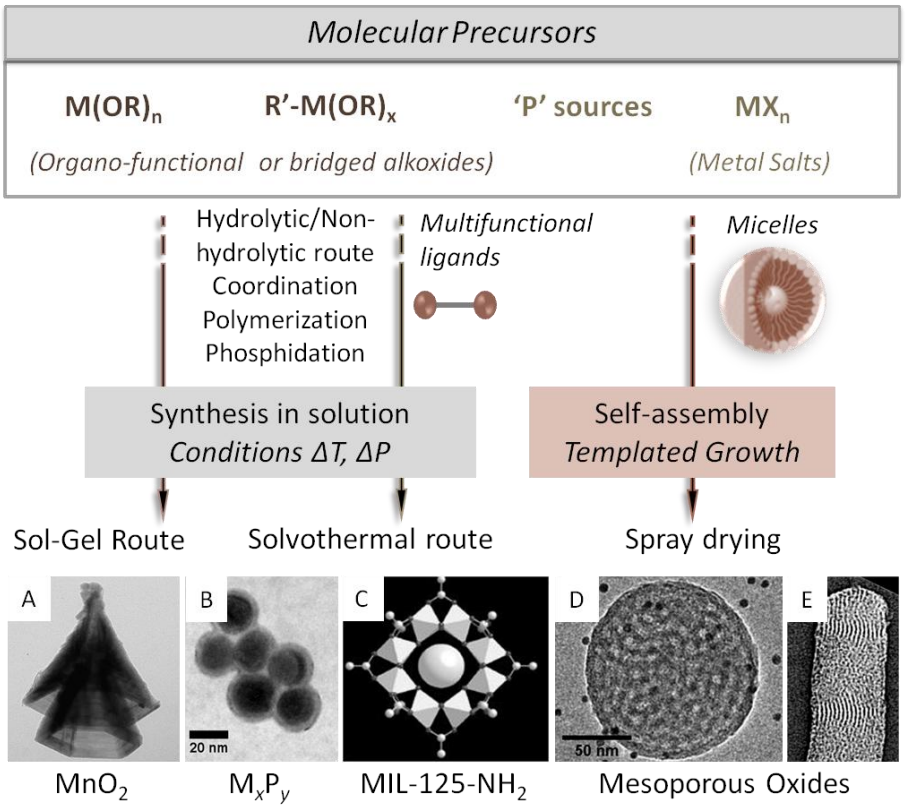

Figure 2: Chemical routes to the nano-objects described in this paper.

First we will introduce the pros and limits of 2D TEM techniques via the structural characterization of a home-made mesocrystal based on nano-heterostructured manganese dioxides. Then the basic principles, performances and limits of analytical 3D TEM will be summarized. Through several examples of functional nanomaterials (aerosol processed spherical mesoporous particles, nanocomposite mesoporous fibers, functional MOFs, and nanometric metal phosphides studied in our group (Figure 2), the following parts of this feature article describe the input of transmission electron microscopy-based methodologies implemented at IPCMS, Strasbourg. We will discuss more specifically analytical tomography that allows probing the chemical composition of 3D nanostructures with nanometer spatial resolution.

1.2 Transmission Electron Microscope: nanoscale objects and interfaces

In parallel to traditional morphological analysis, structural characterization of nanomaterials by TEM was continuously developed, mostly through widely spread techniques like high resolution TEM (HRTEM) and selected area electron diffraction (SAED). Advanced electron diffraction techniques, such as precession electron diffraction (PED) are being implemented into state-of-the-art microscopes,[80] although their use in nanoparticles characterization is mostly uncovered up to now. In addition, the analysis can be performed also in the scanning TEM mode (STEM) using a convergent electron beam that scans the chosen area in a controlled manner. In this case, the transmitted electrons or the electrons scattered at a chosen angle can be recorded for each position of the probe, resulting in images similar to scanning electron microscope (SEM) images but with a resolution which can reach the atomic scale. Note that a significant improvement in the spatial resolution down to the atomic scale was possible by the development of the spherical aberration correctors on the condenser or objective lenses.

Compositional analysis of nanomaterials is now routinely accessible thanks to energy dispersive X-ray spectroscopy (EDS). Depending on the spot size and the imaging mode (TEM or STEM), it is now possible to probe local compositions at the nanometer scale. A significant improvement in the chemically-resolved spatial resolution or in the chemical sensitivity was ensured by the use of High-Angle Annular Dark Field developed in the STEM imaging mode (STEM-HAADF) mode that provides

Z-contrast imaging, Electron Energy Loss Spectroscopy (EELS) and related Energy-Filtered TEM (EFTEM), which emerge in state-of-the-art transmission electron microscopes as techniques for the assessment of materials chemical composition, electronic and optical properties.

Although this article is dedicated to sophisticated and state-of-the art operating TEM modes for the characterization of nanomaterials, it is worthy to recall that most of the currently used microscopes in the field of nanomaterials synthesis consist in traditional tools, which allow simple, versatile and "routine" analysis. Typically, classical TEM relies on a 100-200 kV device, allowing imaging, HRTEM, SAED and EDS analysis. These tools provide 2-dimensional (2D) sample projections, which are certainly sufficient to unravel the morphology and the dimensions of simple objects like nanospheres, nanorods and nanowires. However, when more complex particles are encountered, 2D analysis shows its limitations and some sample preparation "tricks" must be employed.

Manganese oxides provide nice examples of tailored 3D architectures. Indeed, "Chimie Douce" synthesis by precipitation of metal complexes in water below 95 °C yields an impressive collection of nanostructures.[81–83] For instance, by using a seeding approach with initial α-MnO_2 nanowire seeds, a α-MnO_2/δ-MnO_2 nano-heterostructure[82] (Figure 3) could be designed with a 4-fold symmetry cross-like morphology according to scanning electron microscopy (SEM). SAED and HRTEM performed on the "wings" (radial regions) enabled identifying the δ-MnO_2 (LMO) layered structure. Structural considerations indicated that epitaxial growth of δ-MnO_2 on α-MnO_2 (TMO) would yield a 4-fold symmetry as observed by SEM. Nevertheless, α-MnO_2 could not be observed, although it was still present according to X-ray diffraction. To highlight the presence of α-MnO_2 in the core and the relative orientations of the components, thin cross-sections of the nano-crosses were obtained by ultramicrotomy. The analysis of the HRTEM images by Fourier Transform enabled to identify both α-MnO_2 and δ-MnO_2 components and the expected epitaxial relationship.

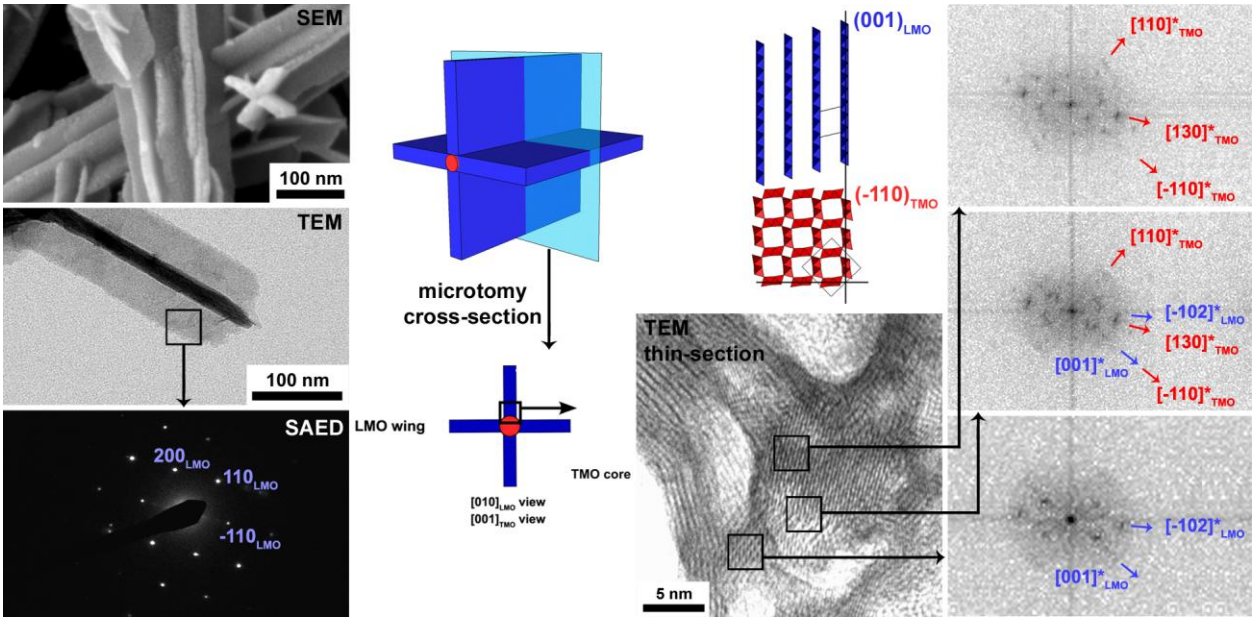

Figure 3: Classical electron microscopy analyses of complex 3D nano-crosses obtained by solvent-mediated seeding. The SEM analysis (*top left*) provides information on the 3D morphology, the TEM image in bright field mode (*center left*) delivers a 2D projection of this morphology, the SAED pattern (*bottom left*) taken on the square-marked area enables to identify the crystal structure of the wings and their structural orientation. The HRTEM analysis of a microtome thin-section (center) followed by Fourier Transform analysis (right) of the different black square areas enables to characterize the 3D morphology, in order to identify the different components and their relative orientations in the nano-object. Adapted from ref.[82]

Other nano-objects can be obtained by self-assembly of nano-building blocks. This is the case of 3D γ-MnO_2 hollow nano-cones (Figure 4).[83,84] For this sample, the SAED mode was an invaluable tool for identifying the orientation of each facet and the twinning planes defining their relative orientations. Still, the growth mechanism involving an initial hexagonal seed and the subsequent oriented attachment of nanorods could only be evidenced by the analysis of particles fragments in microtome thin-sections.

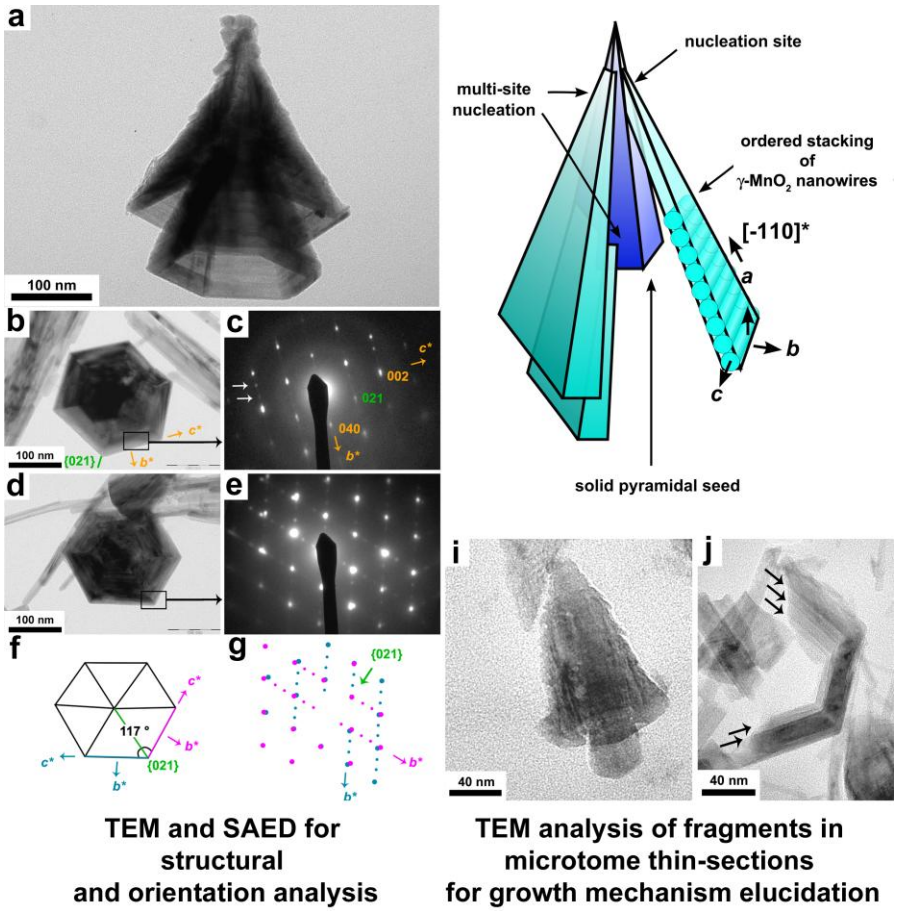

Figure 4: Classical electron microscopy analyses of a complex 3D nano-cone obtained by self-assembly in water. TEM (a, b, d) provides 2D projection of the morphology, SAED (c, e, g) enables to identify structural orientations (f and scheme top right). TEM observations of fragments in microtome thin sections (i, j) provides information on the building-blocks. Adapted from ref. [83] and [85].

In both examples, TEM, HRTEM and SAED allowed morphological and structural characterization of 3D nano-objects by using classical TEM 2D projections. More precise indications of the nanoparticles 3D features were obtained by the combination of SEM imaging and various TEM observations of slices. Nevertheless, this combined approach suffers from severe drawbacks. First, the spatial resolution is worse for SEM than for TEM. Such experiments require expensive high resolution SEM equipped with a field emission electron beam. Second, using two different SEM and TEM apparatuses significantly complicates the observation of the same single object with both techniques. Third, the analysis of thin

slices is not always straightforward, since the orientation of the fragments is reminiscent of the random orientation of the particles versus the blade during cutting. In addition, strains and deformations can result from microtomy, so that care must be taken when considering slices as direct cross-sections of the initial nano-objects. The preparation of thin lamellas by using the Focused Ion Beam (FIB) technique suffers also from similar artefacts.[86],[87] An additional demonstration of intrinsic limitations of SEM or TEM on microtomy slices will be given in section 2 with the example of porous particles. SEM would give only the outer particle topology, while thin sections obtained by ultramicrotomy could not provide information about pore connectivity.

All in all, classical TEM is still in its golden age. It enables in many cases impressive understanding of atomic-scale and nanoscale features, including structure-morphology orientations, interfaces and self-assembly processes. Diffraction-based techniques will not be further discussed, but they will undoubtedly remain essential tools for the characterization of crystalline nanomaterials. Therefore, regular microscopes will certainly stay as invaluable tools in materials synthesis laboratories for most of the fabricated nano-objects, at least for first-hand studies. However, understanding the currently increasing complexity of synthesized nano-objects and their properties requires deeper insight into their 3D organizations and local composition at the nanoscale interfaces. The next sections aim at demonstrating that powerful state-of-the-art transmission electron microscopes are becoming vital analytical apparatuses to answer such questions, especially because they allow bypassing the aforementioned limitations of 2D sample projection.

1.3 Solving the third dimension by electron tomography

The over-increasing interest for the development of new tools able to add the third dimension to the already common 2D methods arise from the fact that the complex nanostructures actually employed for many applications are three-dimensional objects. The current development of electron tomography goes along with the technological advances of electron microscopy.[53],[52] It aims at filling the gap between the synthesis of new materials or structures and the control of their properties at the atomic level. Since

the electron microscopes provide electrons with wavelengths in the picometer range, they are ideally suited for providing 3D information at the nanoscale. For many years, technological issues prevented achieving nanometric resolution at two dimensions, although a description of a mathematical transformation connecting the 3D Cartesian space to its projection onto a cylinder was proposed as early as 1917 by J. Radon.[88] The fast experimental development of tomography occurred only within the recent years, in relation to the development of the computed tomography used in medicine,[89–92] which allowed overcoming the obstacle of developing and applying new reconstruction algorithms. Electron tomography is based on recording series of images of an object, rotated inside the electron microscope, along the widest possible angular range. The construction of a 3D matrix describing the sample in the real space is carried out by applying the inverse Radon transform, which is performed by the back projection of the intensity of each corresponding pixel from the projections into a unique voxel of the matrix being constructed.[93] The main drawback of the electron tomography relates to the angular limitations within the specimen holders and consequently to the finite number of TEM projections, which commonly induce artefacts and distortions in the 3D reconstructions. These issues can be significantly attenuated by applying iterative algorithms. The most popular are the Simultaneous Iterative Reconstruction Techniques (SIRT) and the Algebraic Reconstruction Technique (ART).[94,95] They are based on a sequential comparison between the original projections and that calculated ones at each step of the iterative algorithm. Another new and powerful reconstruction technique is the discrete ART (DART), a method taking advantage of the discrete nature of the reconstructed volumes. It is based on the direct association between the number of grey levels used for the reconstruction and the exact number of components known to be present in the sample under study.[96] As last step of a tomographic experiment, volume visualization and quantification provide insights into the morphology, chemistry and/or phase distribution within the volume.

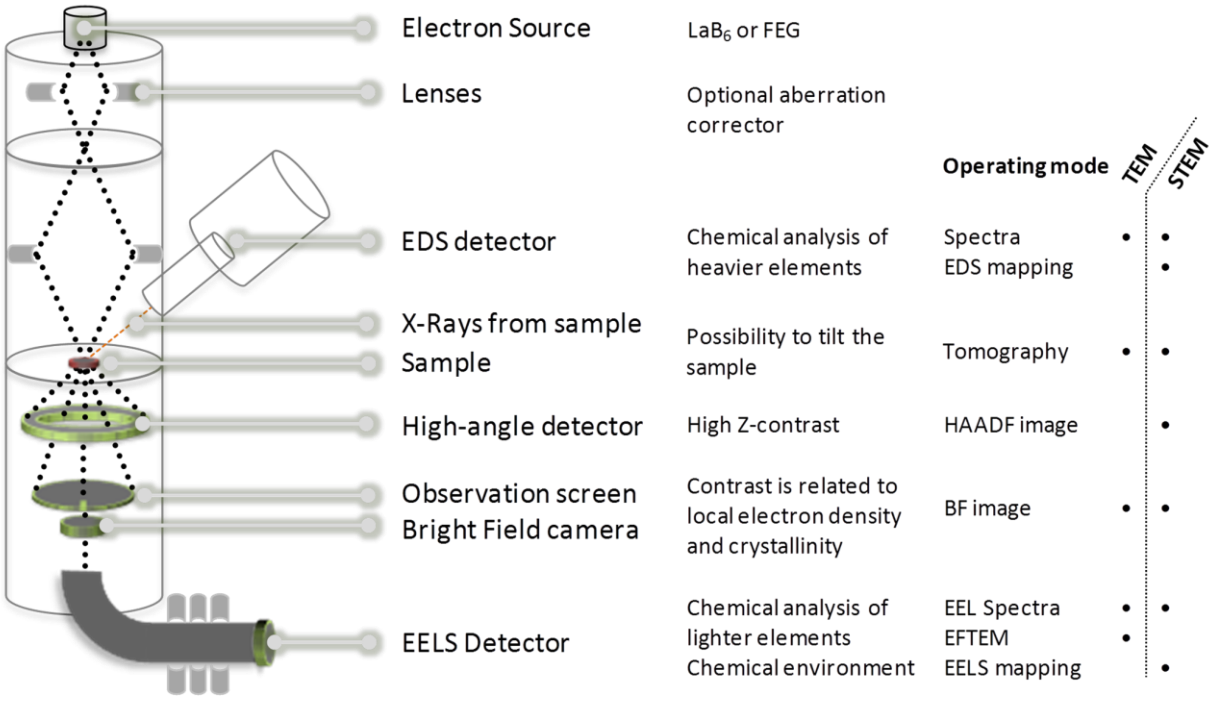

Abbr.	Full name
ADF	Annular dark field
BF	Bright field
ED	Electron diffraction
EDS	Energy-dispersive X-ray spectroscopy
EELS	Electron energy loss spectroscopy
EFTEM	Energy-filtered TEM
FEG	Field emission gun
HAADF	High-angle annular dark field
HRSTEM	High-resolution STEM

Abbr.	Full name
HRTEM	High-resolution TEM
PED	Precession electron diffraction
SAED	Selected-area electron diffraction
SEM	Scanning electron microscopy
STEM	Scanning transmission electron microscopy
TEM	Transmission electron microscopy
Z	Atomic number
ZL	Zero loss

Figure 5: (Top) Schematic representation of a TEM and list of the main acquisition modes. (Bottom) Most common acronyms.

Most of the electron microscopy imaging modes can be adapted to the 3D investigation of nanomaterials, each of them presenting specific advantages and drawbacks (Figure 5). For instance, the requirement of large magnification implies large amounts of data to be collected and processed, with a stringent need for huge computational and storage resources. Aside from this practical aspect, the advantages of tomography experiments are obvious as sub-nanometer resolutions can successfully be

attained, sometimes by using a few amount of the experimental data. For example, very recently alternative approaches based on compressive sensing (CS) or total variation minimization (TVM) have been developed.[97] The compressive sensing considers that a small number of well-chosen measurements can suffice to reconstruct signals that are amenable to sparse or compressible representation. The other crucial goal in electron tomography is to achieve atomic resolution in the reconstructed volumes. Miao et al. recently developed a new reconstruction technique combining equal-slope tomographic (EST) reconstruction with 3D Fourier filtering, allowing to reach the atomic precision.[98,99] Recent advances in electron-based instrumentation, in particular the development of new aberration correctors enable nowadays true atomic-resolution tomography by two methods: i) the recording of series of "confocal images"[100] under STEM mode, well adapted for the analysis of small nano-crystals due to the small depth of field and ii) the combination of STEM acquisition in with a reconstruction algorithm that accounts for the discrete nature of the structure, as applied in general to small nanoparticles.[101,102] However, from a general perspective, coupling classical tomographic approach with electron microscopy imaging modes such as the bright field mode, for example, allows obtaining a larger and better description of nano-objects of interest at three dimensions, from the point of view of their morphology, their crystallographic structure, and their chemical composition.

Initially developed for biology, classical bright field electron tomography was successfully adapted to nanomaterials[103] owing to the strong improvements of electron microscopes in terms of resolution and the ability to process large data flows. This mode is suitable for the study of soft materials such as polymers,[104] amorphous or poorly crystallized specimens such as catalyst supports of complex morphology, containing a nanoscaled active phase (Figure 6).[105] The main drawback of this mode is the presence of diffraction contrast, coming from the active phase, resulting in poor resolution and/or in reconstruction artifacts: such images do not verify the projection requirement for applying the tomography algorithms. The development of new 2D imaging modes in electron microscopy paved the way to the development of more efficient 3D analyses in the nanometer range. For the exploration of nanoscale crystalline materials, the use of the annular dark field (ADF) performed in the scanning mode

(STEM) can remediate the afore-mentioned limitation: the contribution of Bragg diffracted electrons is minimized at high collection angles (HAADF), which makes the images suitable for tomographic reconstruction. Besides, the STEM-HAADF incoherent mode is also known as the Z-contrast 3D imaging mode, since the contrast in the initial images depends mainly on the thickness and local atomic number.[106] This mode is particularly suited for the analysis of samples that contain lighter and heavier elements together.

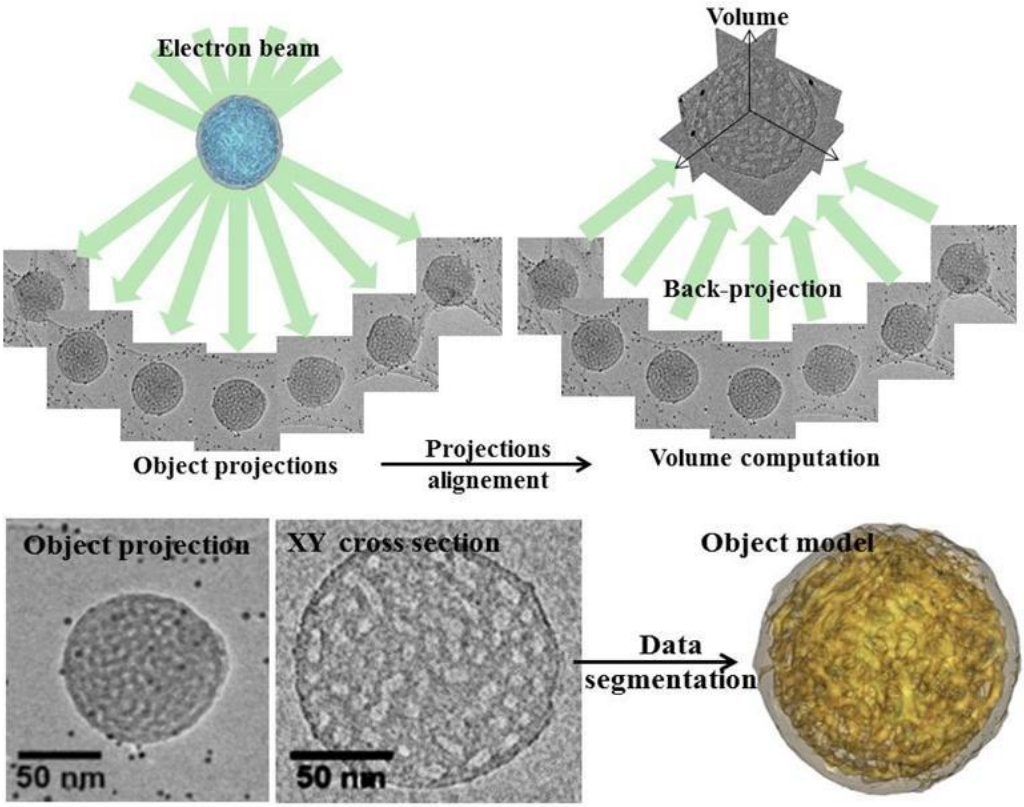

Figure 6: Schematic representation of the electron tomography technique. In a first step a series of projections is acquired while tilting the specimen inside the microscope (*top left*), in a second step the object matrix is constructed using a back-projection algorithm (*top right*). The bottom part illustrates the benefits of passing from a traditional 2D image to a 3D model, in the case of a porous material. The left image is one of the recorded projections, the central one is a slice in the real space through the 3D matrix reconstructed from the projections, while the right shows the 3D image of the object, constructed from the 3D matrix.

1.4 Providing additional selectivity: 3D chemical analysis by EELS spectroscopy and EFTEM imaging

If 3D analytical information is needed, it can indirectly be obtained using the STEM-HAADF imaging mode through the dependence on the atomic number of the tomographic signal. Unfortunately, a large number of materials are made of elements with close atomic numbers, which makes the STEM-HAADF tomography inefficient. In these cases, one of the more reliable ways to achieve 3D chemical mapping is to perform tomography using the energy-filtered TEM (EFTEM) imaging mode.[107–109] This technique combines the ability of the traditional electron tomographic imaging mode to collect 3D information at a nanoscale spatial resolution and the chemical selectivity of the EFTEM imaging mode. It can potentially solve both structural and chemical questions at once. From a practical point of view, it combines the tilt-series approach (reconstruction of a volume from a series of projections) with image acquisition in energy-filtered imaging mode.[110] By choosing the energy windows on the core losses region of the ionization edges of the elements of interest, one can record chemically selective 2D images for a given orientation of the sample (Figure 7). The *modus operandi* is repeated for each tilt angle, giving projection series of the spatial distribution of the elements, from which the 3D elemental maps are deduced. Up to now, this powerful combination did not receive much attention in the field of materials because the EFTEM mode is rather difficult to operate in the tomographic procedure.[111,112]

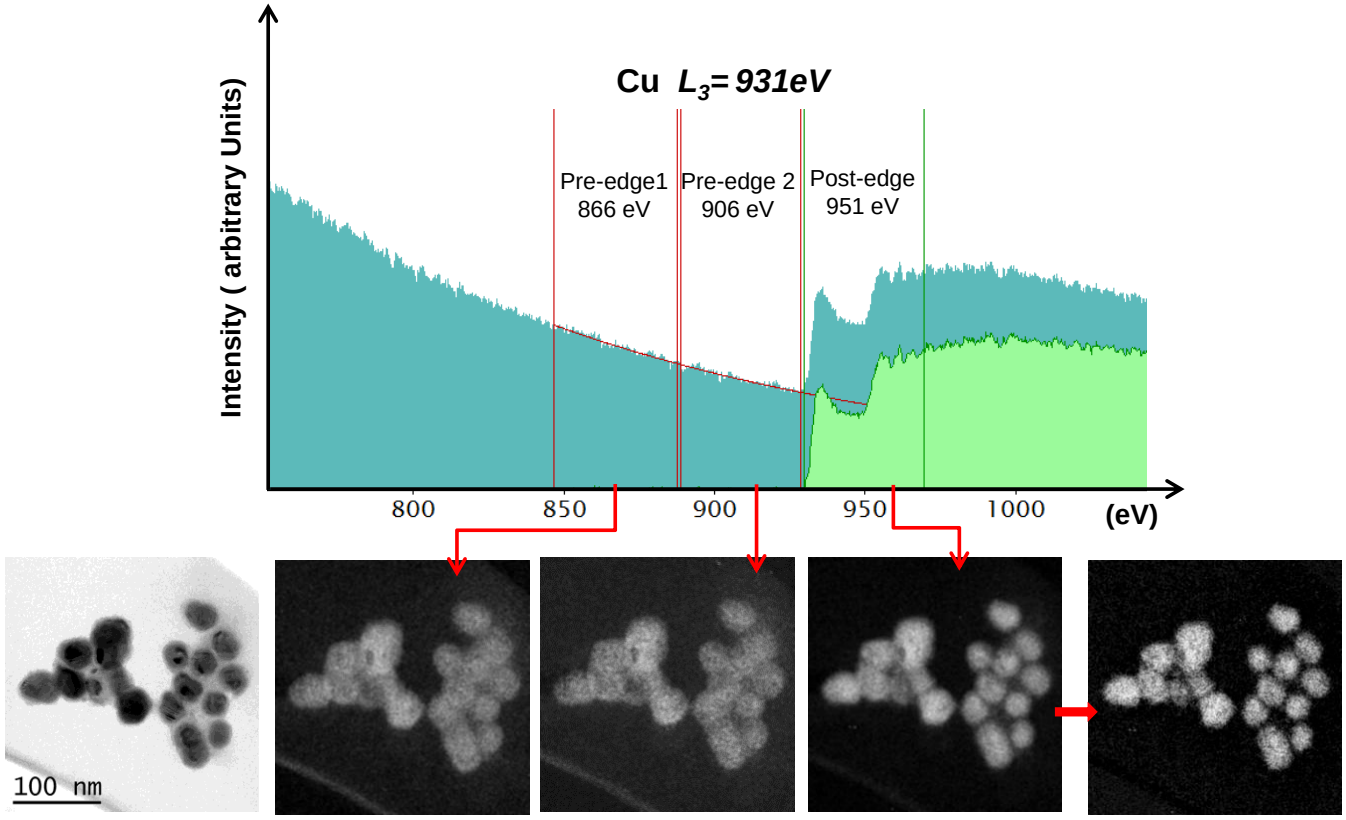

Figure 7: Illustration of the three windows method from an EFTEM analysis on a Cu/Cu_3P aggregate. *Top:* Typical EELS spectra recorded at Cu L_3 = 931 eV ionization edge illustrating the characteristics of the energy windows used to acquire the energy filtered images. *Bottom left:* Image of the Cu/Cu_3P aggregate in the Zero-Loss mode. *Bottom center*: the three energy filtered images ("pre-edge 1", "pre-edge 2" and "post-edge") at the Cu L_3 edge registered for the chosen energy positions; *Bottom right:* elemental projection of Cu obtained after the background extraction.

Another route for probing the 3D chemical arrangement of different species within specific samples is to combine the electron tomography with the EDX spectroscopy.[113] In principle, for each tilting angle, a chemical map is acquired and an EDX spectrum is registered for each position of the beam scanning the sample and for each angle. This approach allows overcoming difficulties such as: requirement of a large magnification, large amounts of data needing to be rapidly collected and processed, new processes needed for combining various bits of information collected on a single sample. Therefore combinations of various modes can be envisaged when studying complex structures.[53,114]

Few examples (reported or unreported) give an illustration of the importance of combining chemical and structural description at the nanoscale. In the following sections, several examples will be discussed: They specifically address situations that would not have been solved by any other tools or combination of tools, showing the unique contribution of transmission electron microscopy and tomography for the design of functional nanomaterials.

2. Mesoporous hollow-shell mixed oxide nanoparticles

2.1 Context

Silica-based mesostructured drug delivery nano-systems have been extensively investigated in the last ten years for they allow a high flexibility of integration of multiple properties needed for efficient imaging diagnosis and/or therapeutic treatments.[115] One of the main issues of these materials is the intrinsic toxicity of the various silica-based cargos which are strongly related to their chemical composition from one side, and to their degradation mechanisms. This last point has been only partially addressed in the literature because it is difficult to investigate *in vivo*. The ideal configuration is to promote a molecular dissolution of the silica matrix, however the large variety of physico-chemical environments (pH, temperature, ionic strength, presence of nucleophilic species, protein adsorption, *etc*.) strongly affects the dissolution kinetics.[116] A well-controlled dissolution kinetic is mandatory but difficult to obtain because the vector architecture can be modified by local silica recondensation[117] (that may affect the drug delivery kinetic as well), or may even promote the random nucleation of very small silica nanoparticles of uncontrolled toxicity in other parts of the body.

In the last five years, our groups conducted an in-depth study in the design of new silica-based nanocarriers with mesoporous architecture able to carry and release progressively large amount of drugs.[118–121] In these works, we developed several methodologies aiming at promoting a progressive molecular dissolution of the silica cargo, while avoiding the saturation of the biological medium in molecular silicic species that would nucleate novel silica particles randomly in the medium. One of the strategies consisted in doping the silica matrix with a few percent of zirconium (up to 20). Aerosol

processing (or spray-drying)[122] was chosen to prepare in one step SiO_2 nanoparticles containing a few percent of zirconia and presenting a very good dispersion and co-condensation of zirconium within the silica network. The nanoparticles were spherical, with a mesostructured core and a dense shell. The seemingly minor modification of the silica inorganic network by zirconium was able to alter very significantly the dissolution kinetic of this drug cargo, and at the same time to regulate the concentration of silicic acid of the medium. Experiments in simulated body fluid showed that 3% of Zr was enough for avoiding silicic acid concentration to reach the threshold for random nucleation of silica particle in the solution.[120] An additional effect was also obtained: the delivery of drugs was delayed.[119] Although these effects were very desirable, their origins were not clear at that moment. Instead, we expected zirconium oxide surfaces to catalyze the fast condensation of silicate species directly onto the cargo, which could in principle promote a progressive rearrangement of the architecture of the cargo (both of the mesostructured core and the dense shell). A very precise 3D morphological investigation of the cargo structure after drug release was thus needed to get mechanistic informations.

2.2 Morphology determination

Owing to the nanometric size of the mesoporous structures, electron tomography was suggested as method for the assessment of pores connectivity, an information that cannot be extracted from nitrogen volumetry measurements. In addition, the complete exploitation of the electron tomography data can give reliable quantitative information on the porous structure of an object. Nanoparticles were analyzed after their exposure to the simulated body fluid. The pores were found to occupy around 20% of the volume of the drug cargo. The mesopores within the silica core presented a mean size of 5 nm and were interconnected with an average length of 10 nm and pores junctions density of 2 junctions/1000 nm^3. This porous network was not directly accessible from the exterior due to the presence of a continuous shell of ca 6 nm thickness at the surface of the particles (Figure 8a and Figure S1). Since in the STEM-HAADF the contrast scales with Z^n (Z: atomic number, n~2), we performed a second tomographic analysis in this mode (Figure 8e). It showed that the shell around the mesoporous core was rich in

zirconia. In addition, small regions richer in Zr were identified locally on the inner pores rims within the silica core (Figure 8f), a clear indication of the Zr diffusion from the surface regions to the core.

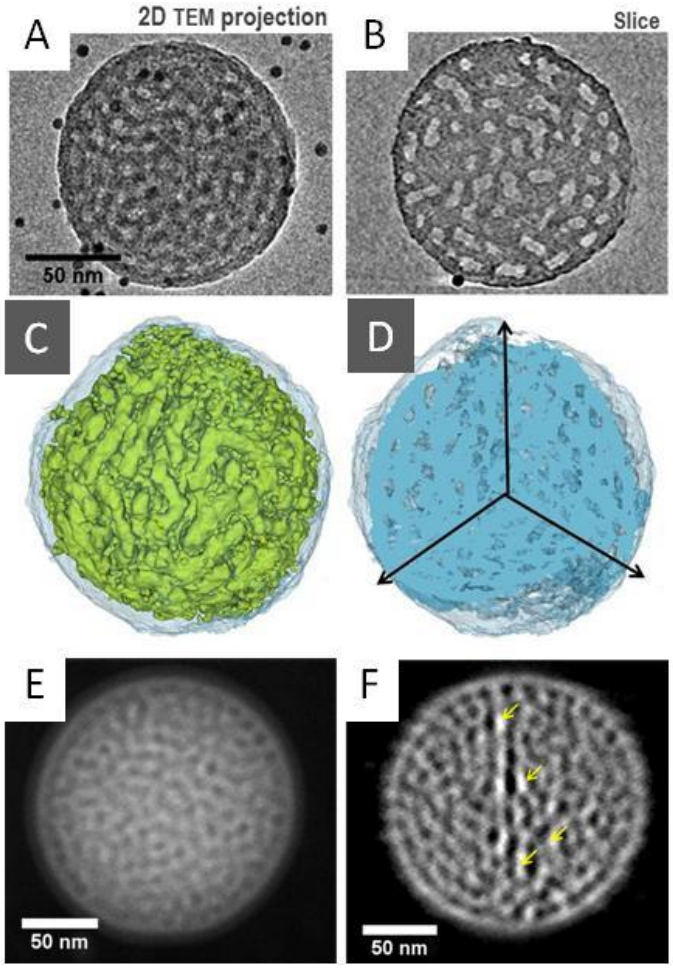

Figure 8: 3D analysis by electron tomography in the TEM (*top*) and STEM-HAADF (*bottom*) modes, for a mesoporous SiO_2-ZrO_2 oxide NPs used as nano-carriers. A) TEM image at 0° tilt extracted from the tilt series; B) Typical slice through the reconstructed volume; C) 3D model of the object, with the porous network in green and the silica-based material in blue. D) Typical orthogonal slices through the 3D model showing that most of the mesopores are not accessible from the outside part of the particle. E) STEM-HAADF image extracted from the tilt series used to reconstruct the Z-sensitive volume. F) Typical cross-section through the Z-sensitive volume, showing the distribution of the zirconia-rich area (slighty brighter, due to the higher atomic number of Zr *vs.* Si): some of them are in the shell of the particle while others are in the areas pointed by arrows.

Altogether, combined electron tomography in TEM and STEM-HAADF modes evidenced the influence of zirconium on the silica mesoporous structure: a continuous shell was identified around the particles and the pore connectivity was fully characterized, explaining the delay observed for drug release as well as the robustness of the cargo regarding dissolution.

This study stands as an example of detailed analysis of a mixed oxide structure that presents porosity and an non-homogeneous chemical distribution of elements. In the next section, the case of hybrid organic-inorganic fibers containing metallic nanoparticles is discussed.

3. Mesoporous inorganic and hybrid fibers: intricate morphologies

3.1 Context and motivation

Being able to precisely locate organic functions within organic/inorganic hybrid materials is an important challenge for many functional material applications. The functional groups (and associated properties) provided by grafting, coating or direct incorporation, are of main interest for the preparation of multi-functional materials. Moreover, the specific position of a functional group in the material microstructure addresses a specific property which strongly depends on its localization: on the surface, within the porosity, inside the inorganic matrix, etc.

The design of efficient membranes for proton exchange membrane fuel cells (PEMFC) typically rely on the adequate positioning of conductive groups. In the study described below, determining the topological distribution of thiols - a precursor for forming proton-conducting sulfonate groups - within hybrid silica nanofibers was critical, because proton transport and the accessibility of the fibers porosity strongly depend on it.

Silica mesoporous fibers were prepared from a sol-gel route.[123] Efficient functionalization with thiol groups was confirmed using FTIR spectroscopy. The S-H stretch absorption was detected at 2550 cm^{-1}, and shifted to 2572 cm^{-1} after washing of excess thiol and remaining surfactants. FTIR experiments strongly suggested that the thiol groups were mainly located on the surface of the mesopores and not on the external surface of the fibers, because of the lower vibration frequency observed before the washing

step: it was likely due to favourable interaction of mercaptopropyl groups with the surfactants located inside the mesopores. However, this needed proof.

3.2 Strategy for labeling the mercapto groups

Our strategy to detect these poorly-contrasting mercapto groups was to use metallic gold nanoparticles as high-contrast trackers: they were expected to graft onto the mercapto groups present on the silica. Alternatively, the mercapto groups could be used as nucleation points for the *in situ* growth of gold NPs from dissolved gold salts. The synthesis of gold@SiO_2 fibers was investigated following these two routes: (i) post-synthetic grafting of commercial nanocrystalline gold NPs (diameter of 5 nm) and (ii) *in situ* generation from gold salts after the synthesis of the hybrid fibers, by reduction under hydrogen.

The morphology and distribution of Au NPs in the mesoporous silica fibers were directly observed by TEM in both cases. In route (ii), the mesoporosity was slightly disrupted because of the high content of Au NPs: the average pore size was 2.3 nm and the gold NPs formed randomly and with a high dispersion within the material. On the contrary, colloidal gold with a diameter (5 nm) larger than the mesopores (ca 4 nm) was chosen in route (i). The NPs were added in ethanol suspension of the silica nanofibers in order to target the mercaptopropyl groups of the outer wall-surface of the fibers. In this latter case, the mesostructure of the gold post-grafted samples remains undamaged and only a weak amount of gold particles was grafted on the external surface of the fibers. For both routes, electron tomography was instrumental in determining if the NPs were located on the surface or within the pores of the silica mesoporous fibers. We discuss below the detailed analysis of a sample prepared according to route (ii).

3.3 Electron tomography on 3D mesoporous fibers

The slice-by-slice analysis of the reconstructed volume clearly showed the occurrence of Au NPs within the mesopores that presented a mean diameter of 4.5 nm. A more detailed analysis of the 3D positions of the resulted particles highlighted a rather homogenous distribution of the thiol groups (marked by the presence of gold NPs) amongst the different pores of the fiber (Figure 9 and Figure S2). Unexpectedly, the mesopores seem to present an helicoidal orientation along the longitudinal axis of the

fiber, as suggested by analysis of the NPs distribution belonging to the same pore (Figure 9, right). Some small connections between the pores and the outside can be periodically observed, as illustrated in Figure 9 (center).

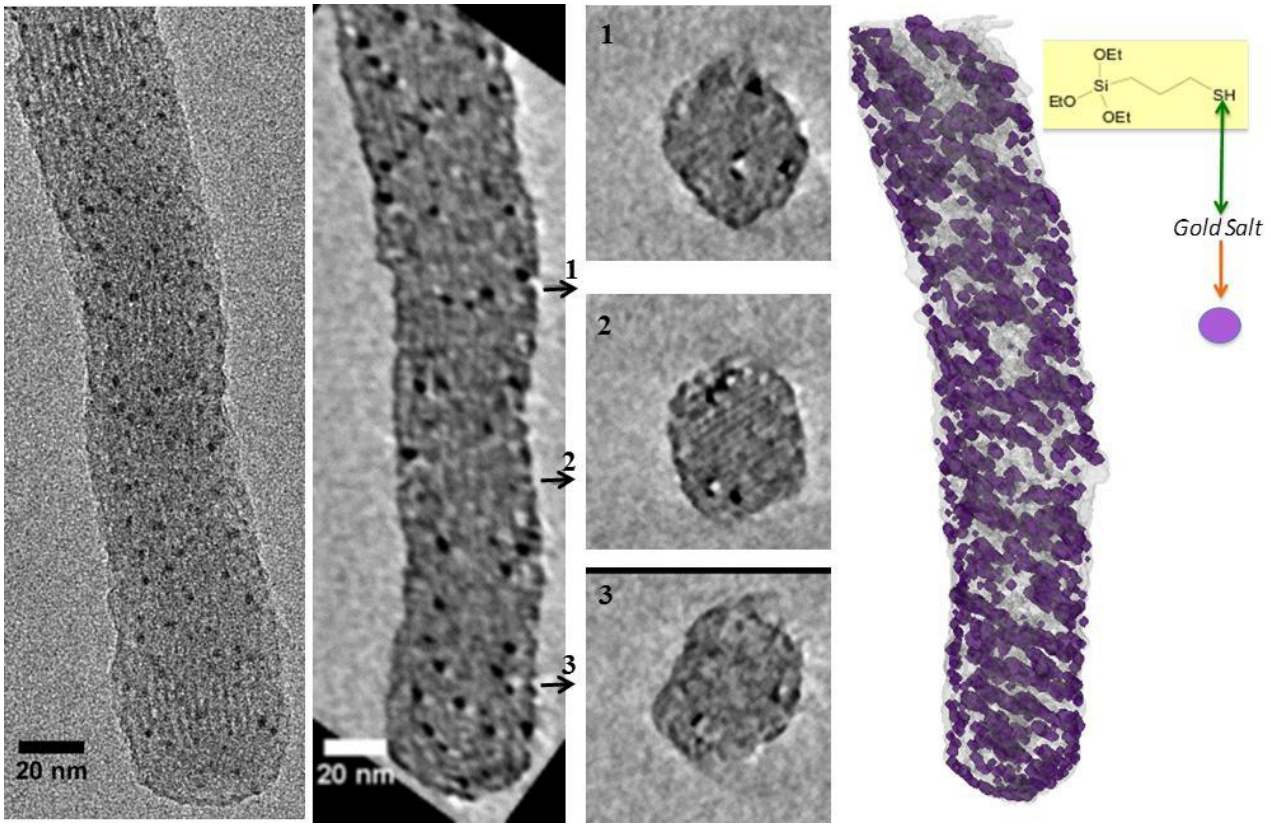

Figure 9: 3D-TEM analysis of the mesoporous silica fiber inside which gold nanoparticles were grown. *Left*: Typical 2D TEM projection extracted from the recorded tilt series used to reconstruct the volume; some ordered and well oriented parts can be observed periodically along the fiber, suggesting a periodical change in the pores orientation. *Center*: One representative longitudinal slice and three transversal slices at the positions 1, 2 and 3, through the reconstructed volume. Their direct analysis illustrates the positions of the gold particles within the pores and connections of the external pores with the outside. *Right*: 3D reconstruction of the whole object with the Au particles in purple and the silica fiber in gray.

These findings supported that the mercapto-groups were mainly located inside the silica fiber mesopores. The 3D reconstruction also highlighted an unexpected helicoidal structure of the porosity

within the fiber. These two features observed on the complex architecture of these mesoporous silica fibers are typical examples of the contribution of electron tomography to in-depth nanomaterials analysis.

The two cases discussed so far (silica-zirconia particles and silica fibers) illustrated the power of electron tomography when it comes to analyzing inorganic, highly contrasting structures (though using Au NPs as markers actually provided information on the topological distribution of mercapto groups). The next example will be focused on mapping directly the organic moieties of nanomaterials.

4. Titanium-based MOFs: Solving the amino group distribution within a hybrid network.

4.1 Context and motivation

Metal-organic frameworks (MOFs) are a class of materials composed of organic and inorganic building blocks.[124–127] These highly ordered and porous networks are of interest for their applications in gas storage, catalysis, photo-active materials...[128–135] Some MOFs have the ability to behave as semiconductors when exposed to light, making them unique platforms for light harvesting and photo-induced catalysis. A subfield of research has thus emerged with the aim of tuning the optical response of MOFs by modifying the inorganic unit or the organic linker (length, chemical functionalization).

In this context, the highly porous titanium-based MOF MIL-125 is an interesting candidate. This material, which contains cyclic octamers of TiO_2 octahedra, is photochromic, which is related to the reduction of Ti(IV) to Ti(III) under UV irradiation (Figure 10a).[136] When synthesized with 1,4-benzenedicarboxylate (bdc) as an aromatic linker, MIL-125 has an optical band gap in the UV region (ca. 3.6 eV/345 nm) and is an active photocatalyst for the oxidation of alcohols to aldehydes.[136,137] Nowadays, amine linkers are becoming particularly popular for porous MOF, because the polar -NH_2 groups are expected to enhance CO_2 capture performances, while allowing selective gas adsorption and enabling post-synthetic modifications.[138–140] The iso-structural MIL-125-NH_2 was prepared using a modified bdc-NH_2 linker (Figure 10b). It was reported to be a photocatalyst with visible-light-induced activity for CO_2 reduction[141] and H_2 production.[142] Moreover, the bdc-NH_2

linker was shown to be responsible of an extra absorption band in the visible region, indicative of the reduction of the band gap (ca. 2.6 eV/475 nm).[141–143]

4.2 Design of an amino-functional MOF

In order to take advantage of the crucial role of the -NH_2 group in the band structure of MIL-125 compounds, MOFs derivatives with mixed bdc/bdc-NH_2 linkers were synthesized in a one-pot route from inorganic molecular precursors and the mixture of the two organic linkers (in 90/10, 80/20, 50/50, 33/66 molar ratio). The optical response of MIL-125 can be tailored toward absorption in the visible region through rational selection of amino substituents of the aromatic bdc linker. The impact of the electronic modifications induced by the aromatic moieties of bdc in MIL-125-NH_2 was confirmed by DFT calculations.[144] Moreover, the functionalization of the internal surface of a MOF can reduce its pore size because the additional functional groups fill up the pores. Therefore, the ratio of bdc-NH_2 ligand was optimized to preserve the parent structure, to promote maximum porosity, and to tune the optical band gap of the MOF.[145]

From an experimental point of view, X-Ray diffractograms of MIL-125, mixed bdc/bdc-NH_2 MIL-125 and pure MIL-125-NH_2 are strictly the same. It is thus not possible to know if the mixed bdc/bdc-NH_2 MIL-125 sample is a macroscopic mixture of the two phases (i.e., with a segregation of the two linkers), or if the linkers are randomly dispersed inside the MIL-125 structure. A local characterization technique with chemical sensitivity and a resolution in the nm range was thus required to map the nitrogen at the nanoscale.

4.3 Characterization of amino groups dispersed in the MOF

Classical STEM-EDS mapping would have been inefficient here because nitrogen is a light element. On the contrary, EELS allows the detection of nitrogen at its K-edge (401 eV) inside the MIL-125 structure, which is mainly constituted of superimposed plate-like grains, as observed on the bright-field micrograph of Figure 10c. An EFTEM study was performed in order to explore the microstructural features within this specimen and to assess the distribution of the amino ligands, which was compared with the distribution of titanium species, also mapped in EFTEM using Ti $L_{2,3}$ edge (456 eV). This

chemical analysis revealed that both the titanium and the nitrogen uniformly distribute on the MIL-125 structure at the nanoscale (Figure 10d). This information was a key for explaining the system specific optical behavior.

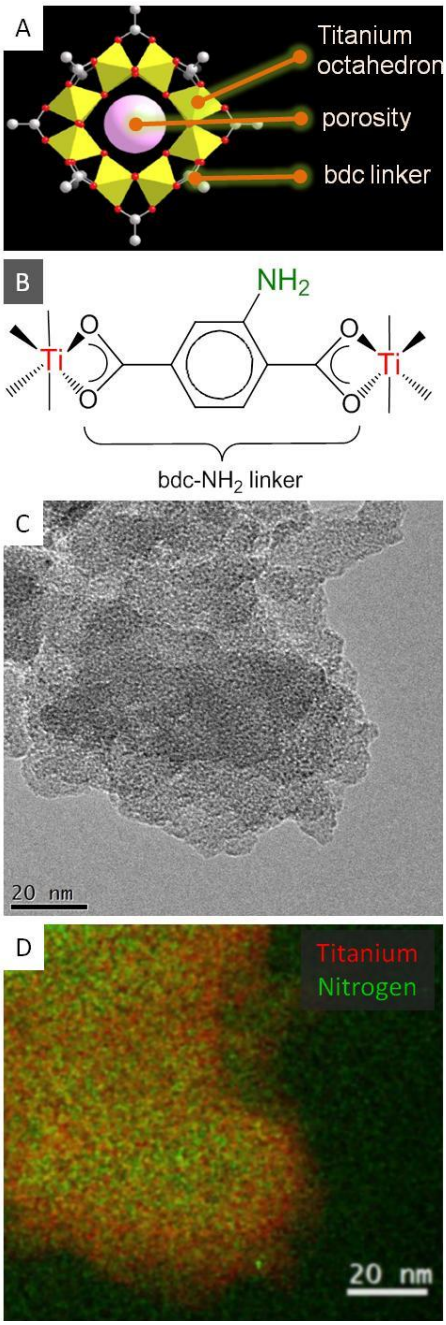

Figure 10: A) Structural unit of MIL-125; B) Structure of the bdc-NH_2 linker; C) Classical TEM image of MIL-125 obtained with mixed organic linkers (bdc/bdc-NH_2 in a 50/50 ratio); D) Relative chemical map, with titanium in red and nitrogen in green, obtained from a 2D chemical EFTEM analysis,

illustrating the relatively good homogeneity of the nitrogen in the material. The resolution of the map is 2 nm.

This example highlighted the capability to probe the local distribution of an organic moiety within an hybrid functional materials. It was critical to perform such analysis with a resolution down to the nanoscale in order to prove that there was no segregation within the structure. Moreover, EELS was mandatory for detecting nitrogen, which is a light element. In the next series of examples, another light element, phosphorus, will be at the heart of the structural and chemical questions related to the design of metal phosphide nanoparticles.

5. Metal phosphide nanoparticles: where is the phosphorus?

5.1 Context and motivation

Metal phosphides (M_xP_y) are covalent materials with applications in various fields such as metallurgy, semi-conductors for electronics, or optics. Traditional preparation routes employed solid-state high temperature approaches, which precluded the formation of well-controlled nanocrystals.[146] However, during the last two decades, solution routes to nanoscaled metal phosphide have been extensively developed, allowing for the formation of a wide set of metal phosphide nanoparticles (eg. Ni_2P, CoP, InP, PdP_2, etc.).[147] This opened an avenue for studying surface-related properties such as catalysis: hydrogenations of unsaturated bonds and hydrodesulfurization (HDS) have been particularly developed.[148] The presence of phosphorus not only changes the intrinsic properties of the bulk lattice,[149] such as the band levels, but it also affect the reactivity of their surface: for example, phosphide surface species were found to limit the sulfur poisoning during HDS,[150] while they also favored semi-hydrogenation of alkynes into alkenes instead of full hydrogenation to alkanes.[151] Phosphorus surface species were also suspected to be responsible for the unexpected selectivity of a nickel-cobalt catalyst for CO_2 reduction by H_2.[152] A correct interpretation of the properties of metal-phosphorus nanocomposites thus requires to locate the phosphorus species.

Our group developed a low-temperature stoichiometric route to metal phosphide nanoparticles. It is based on the reaction of metal(0) nanoparticles (eg. Ni, Pd, In) with a highly reactive, soluble source of elemental phosphorus: white phosphorus (P_4).[153,154] This insertion reaction has the advantage of being stoichiometric in most cases (all the phosphorus from the solution gets inserted into the nanoparticles), even at fairly low temperatures (r.t. to 200 °C),[155] meaning that restructuring of the nanoparticles upon the formation of novel crystalline phases can be followed as a function of energy input (here, the reaction temperature).[156] While XRD and other structural methods allow for an easy identification of the resulting crystalline phase, local composition measurement was critical to understand the synthetic processes that often proceeded through intermediate amorphous phases.[157]

5.2 EELS in 2D: solving some of the structural questions (Pd-P, Cu-P, Au-P)

Such information is exclusively accessible through chemical analysis by TEM. Phosphorus being a fairly light element, EELS was preferred to EDS for the analysis of Pd-P,[157] Cu-P[155] and Au-P[158] nanostructures. In this latter case, EDS could not be considered anyway, since the Au and P ionization edges overlap enough and cannot be properly resolved with standard detectors. In these examples, phosphorus was only present as phosphide species: EFTEM was able to unravel the chemical structure, and in particular the localization of phosphorus.

As a representative example, the case of copper phosphide is discussed below. Nanoscaled copper phosphide can be prepared with two stoichiometries: Cu_3P and CuP_2.[155] Using preformed copper nanoparticles reaction with P_4, in a molar Cu:P ratio of 3 and 0.5, respectively, we showed that, within 2 h at 250 °C, the insertion of P into the nanoparticles was quantitative, yielding as expected Cu_3P and CuP_2 nanoparticles, respectively. However, we also noticed that in milder conditions (100 °C) and after shorter reaction time (30 min.), the insertion of P was not complete but crystalline Cu_3P could already be observed by XRD, in addition to the remaining crystalline copper.

2D analyses by EEL spectroscopy have been performed, using the EFTEM imaging mode. The elements of interest were phosphorus with the $L_{2,3}$ = 132 eV ionization edge, copper with L_3 = 931 eV ionization edge and oxygen with K = 532 eV ionization edge. The corresponding EEL spectra are given

in Figure 11 (left). The 2D chemical maps of the three elements were obtained using the three windows method in order to have a proper background removal from the total inelastic signal (Figure 11 right). A better visualization of their relative distribution is obtained on color-coded 2D elemental maps (Figure 11 center) that shows the core-shell structure of the nanoparticles, with a core exclusively made of copper and a shell constituted by Cu_3P (partially oxidized on the surface due to air exposure).

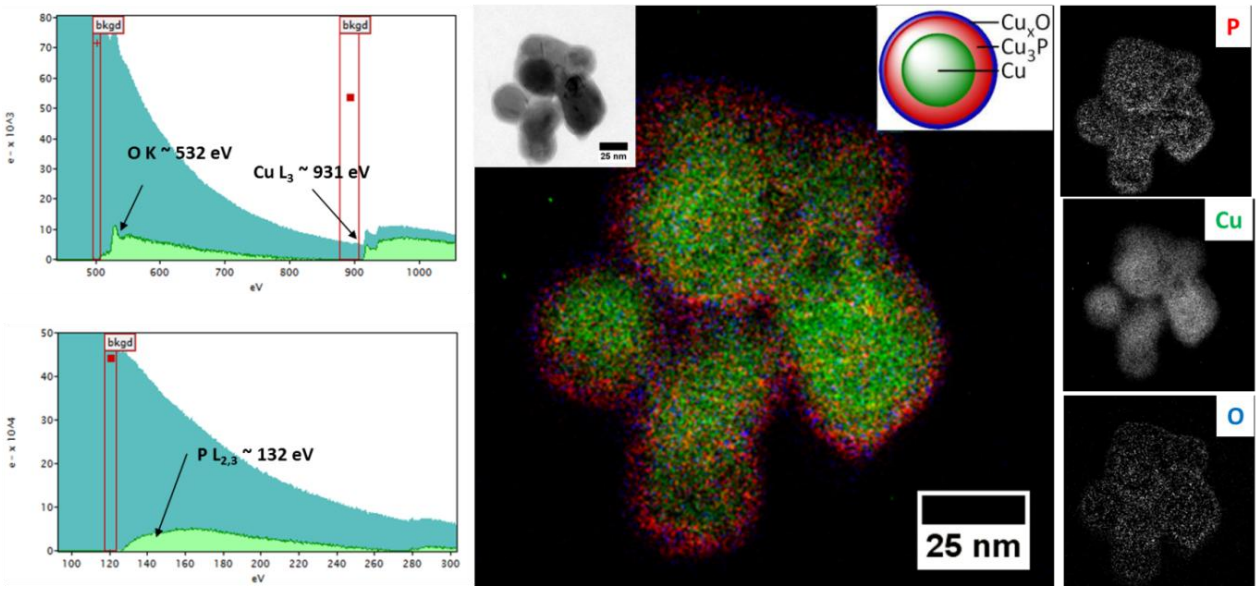

Figure 11: Core shell structure of copper phosphide nanoparticles: *Left:* Typical EELS spectra registered on the Cu and P ionization edges. *Center:* 2D relative map of the studied object with phosphorus in red, copper in green and oxygen in blue. The left inset shows the TEM image of the nanoparticles. The right inset is a scheme of the particles structure. *Right:* elemental projections for each element obtained after background extraction, using the three-window method.

This measurement allowed understanding the mechanism of the reaction: contrary to most other cases encountered in metal phosphide synthesis, for copper phosphide the crystallization occurred immediately upon phosphorus insertion. Instead of yielding as usual an amorphous structure, incomplete P insertion formed a core-shell crystalline structure with the phosphide in the shell.

5.3 Multiple phosphorus species in Ni-P nanoparticles: the need for 3D chemical mapping

As explained above, our synthesis of metal phosphide nanoparticles rely on preformed metal nanoparticles. In the case of nickel, well-calibrated nanoparticles are most efficiently obtained using a

phosphorated surface ligand, the tri-n-octylphosphine (TOP).[159] This raises an additional issue for the chemical characterization of Ni-P species: not only is there phosphorus inside the particles as phosphide, but remaining phosphines (or their oxide when the sample was exposed to air) are still around the inorganic core. Nevertheless, the study of magnetic and catalytic properties of these types of nanoparticles required a similar structural resolution than those of Cu-P nanoparticles. The experimental observation for Ni-P nanoparticles was the following: insertion of 0.33 equivalents of P into monodispersed Ni nanoparticles did not yield crystalline Ni_3P nanoparticles. Rather, a nanocomposite of crystalline Ni_2P/Ni was formed, through an amorphous intermediate. In terms of magnetism, we observed that lowering even more the stoichiometry of phosphorus to a Ni:P ratio of 4 resulted in an increase of saturation magnetization.[160] For catalysis, the composite structure was found to have alkynes hydrogenation properties similar to those of Ni nanoparticles at low temperature, and to those of pure Ni_2P nanoparticles at ca 200 °C.[151] Both the magnetic and the catalytic properties demanded an in-depth analysis of the phosphorus localization in the nanoparticles.

They presented a diameter of ca 25 nm and were mostly spherical. In this case, 2D chemical analyses may not be sufficient to solve the spatial distribution of chemical species. In this context, the use of the analytical tomography by EFTEM imaging is appropriate for providing chemical information, in particular to corroborate the following hypotheses: the absence of the phosphorus in the nickel shell and its homogenous distribution within the core. Concerning the first one, attesting the phosphorus absence within the shell by using the EFTEM tomography approach is clearer than when using the 2D chemical maps, due to a better signal to noise ratio (SNR) in the reconstructed volume associated to the redundancy of information coming from the use of several adjacent images.[161,162] Concerning the phosphorus distribution within the core, it is more pertinent to analyze slices extracted from the 3D chemical reconstruction than 2D chemical maps in which the thickness effect is present.

5.4 EFTEM tomography for element-sensitive volume reconstruction

The chemical composition of the nanocomposite was solved by EFTEM tomography by considering the P $L_{2,3}$ = 132 eV ionization edge (inset of Figure 12) with the acquisition of the energy filtered

images at low temperature using a cryo-holder to prevent the irradiation damages in the specimen previously observed in the case of tilt series acquisitions at room temperature. Note that, as the plasmon region is not far from the P $L_{2,3}$ edge, the three windows method was no longer appropriate for the extraction of the P chemical signal. Accordingly, we considered another method for the signal extraction which uses only two filtered images, one before and one after the P ionization edge, as proposed in the literature for the elemental mapping of the P element.[163,164] In our case, their characteristics (width and positions) are illustrated in the inset of Figure 12, where an EELS spectrum acquired on an assembly of six Ni_2P/Ni nanoparticles is shown. The corresponding elemental projections recorded at the same angle are shown in Figure 13 right. More details on the experimental protocol and data treatment procedure used for the calculation of the P elemental projection tilt series are given in the Supporting Information.

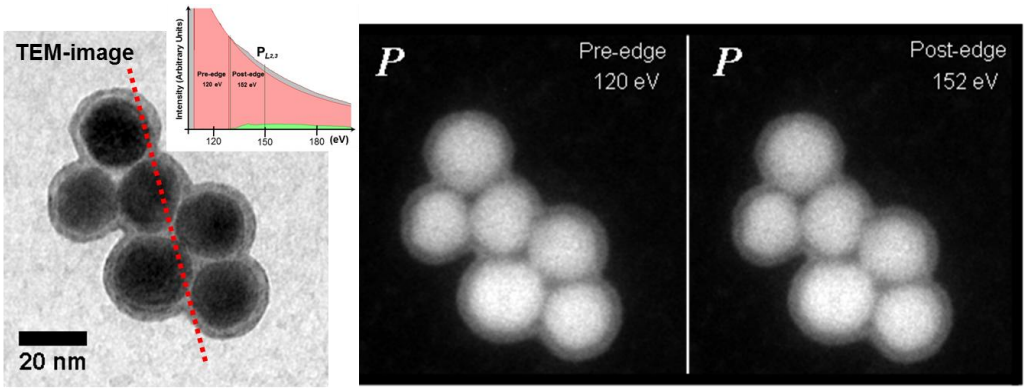

Figure 12: *Left:* Typical image from the "Zero Loss" tilt series acquired in EFTEM on the object chosen for the tomographic study; the red line indicates the position of the tilt axis. Inset: global EEL spectrum, illustrating the positions and the widths of the two energy windows used for the acquisition of the two energy filtered tilt series on the P-$L_{2,3}$ ionization edge. *Right:* The two energy filtered images registered at the same angle before (120 eV) and after (152 eV) the P-$L_{2,3}$ ionization edge.

Using the Zero Loss and the P chemical projection tilt series as inputs, the reconstruction algorithms allowed computing two spatially correlated volumes, corresponding to the mean density distribution and to the P chemical volume. By superposing the two volumes pixel by pixel, we obtain a 3D "relative" map, which reflects the relative variation of the P signal inside the particle. Figure 13 (right) shows

longitudinal sections extracted at the same depth from the two reconstructed volumes, mean density and P chemical maps respectively.

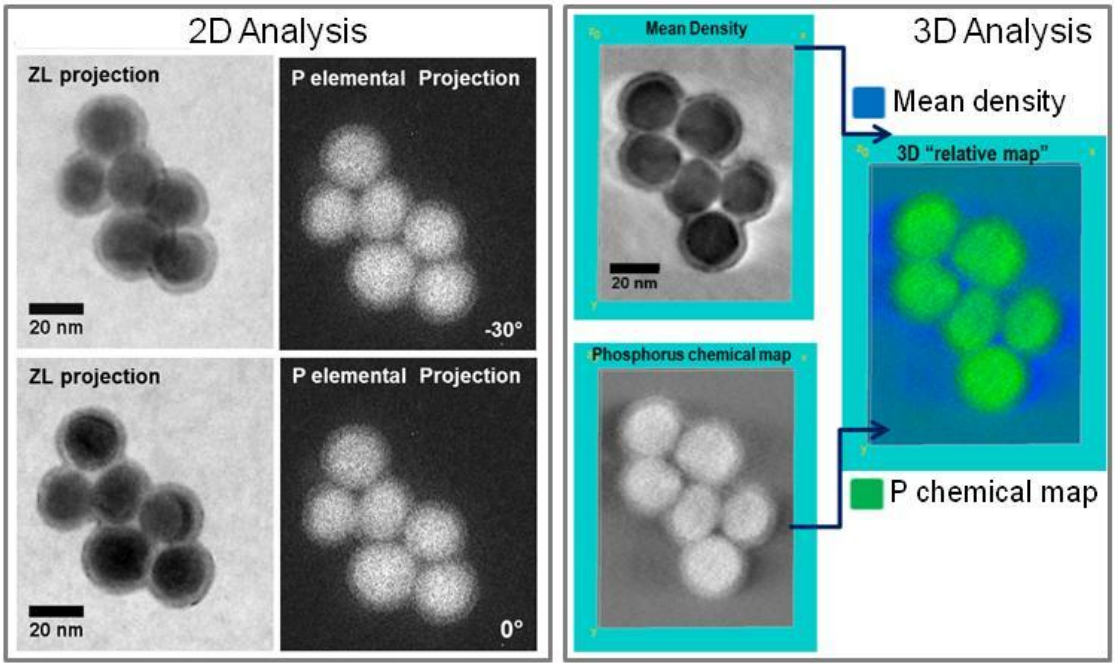

Figure 13: Outputs of the reconstruction algorithm. *Left:* Typical projections extracted at two different angles from the Zero Loss-tilt series and the P elemental map tilt series. *Right:* Longitudinal sections extracted at the same depth and orientation through the three reconstructions: the mean density reconstruction, the P 3D chemical map and the 3D "relative" map obtained by superposing the two previous reconstructions (phosphorus in green and mean density in blue).

The combined analyses of the three reconstructions provide reliable information on the nanoparticles morphology and interface features. We have confirmed that the NPs present a spherical shape with a chemically and morphologically well-defined shell surrounding the core. Given the difference in the "P intensity" between the core and the shell, we can now conclude that the P is not present in the shell and it is homogenously distributed within the core. Note that, once again, though similar information can be deduced from the classical 2D chemical maps, the analysis of a 3D reconstruction is more relevant because the thickness effect is not present. These findings are in agreement with the postulated existence of a 3D core-shell structure with crystalline Ni_2P located in the core, as a result of a spontaneous phase segregation of amorphous Ni_3P into crystalline Ni_2P (core) and Ni (shell).

From a more general point of view, 3D EFTEM allowed a detailed and reliable analysis on a fairly beam-sensitive sample, which fueled in-depth discussion on the relative stability of covalent inorganic compounds at the nanoscale.[156] This study underlines the efficiency of low-temperature analytical tomography for sensitive materials, as an approach that can be implemented on last generation electron microscopes.

6. Towards the direct observation of materials behavior in their natural and/or functional environment

In the examples above, samples were analyzed in a static fashion, under ultra-high vacuum, with no external stimuli applied, such as heat,[165] light,[166] chemical reactant through liquid[167] or gas phase.[29],[168] A sustained trend of the last decade precisely deals with the introduction of such capabilities in modern TEM. These allow *in situ* analysis of complex materials in a medium that is closer to their standard environment in a device or a catalytic reactor. From the point of view of materials, dynamic behavior can now be monitored at the atomic scale.[169]

The field of environmental TEM in liquid is particularly active, with several technological solutions been developed worldwide.[167,170] Many energy-related questions such as the improvement of lithium batteries or the optimization of electrocatalysts will be best addressed by monitoring the behavior of nanoparticles into liquids. Moreover, in solvothermal synthesis, the very birth of nanoparticles (nucleation, growth) and their further evolution (ripening, aggregation), occur in a liquid medium. A recent work by Zhu et al. illustrates the rotation and diffusion of Pd nanoparticles in an aqueous solvent, with atomic resolution.[171] Growth and shape evolution of FePt nanoparticles in organic solvents was also investigated: shape evolution was followed in real time, and a critical concentration of oleylamine surfactant could be determined for the stabilization of nanorods.[172] Altogether, environmental TEM is opening a new age for TEM as it gives not only a snapshot, but a dynamic understanding of functional nanomaterials. Beyond the inputs that can be expected in energy storage and conversion research as well as in biology or catalysis, one could dream of implementing these new characterization techniques directly in the production line of nano-materials, as a guide for their design.

7. Conclusion and outlooks

For the last years, the materials science community oriented its efforts towards the synthesis and development of new materials with properties defined at the nanoscale. Probing at two or three dimensions the nanomaterials structural, chemical and morphological features was challenging. The problem was addressed anew by taking advantage of technological advances in the field of electron microscopy. The technique's power relies not only on its imaging capabilities, but also on its ability to chemically describe complex nanostructures with nanometer spatial resolution. The third spatial dimension could be added to the existing 2D observations only in the early 2000's, when the computational developments allowed the set-up and implementation of iterative procedures for volume reconstruction. Today, electron tomography stands as the only technique that can decide without a doubt whether nano-objects lie inside or outside a hollow structure, and that can satisfactorily assess the morphology and/or faceting of nano-crystalline structures. Moreover, the challenge of quantitative tomography was tackled by combining it with the various modes available on a modern TEM, providing even more precise information about morphological, structural and/or chemical characteristics of several nanocomposites.

Electron microscopy has been successfully adapted to complex systems for assessing their porous characteristics, chemical homogeneity and/or species distribution at two or three dimensions. Two relevant examples described above, the mesoporous nanoparticles and fibers, highlight the benefits of electron tomography for exploring both the porous network topology (size, connectivity, etc.) and the distribution of foreign chemical species that provide additional functions within a 3D complex system. When an energy loss spectroscopy expertise is combined to TEM imaging (energy-filtered imaging), the chemical homogeneity of the hybrid structures can be resolved, as shown for the titanium based metal-organic frameworks. At the opposite side, the chemical in-homogeneity of complex nanostructures requires a 3D approach: the analytical tomography. By associating the energy-filtered imaging with the tomographic approach, the analytical tomography allows to probe the chemical composition of 3D nanostructures with nanometer spatial resolution. As applied to the case of metal phosphide

nanoparticles, the 3D relative elemental distribution identified a core-shell morphology dominated by the presence of crystalline metal phosphides in the core, as result of the phase segregation from an amorphous intermediate. All these examples prove that the close correspondence between morphology and chemical composition stands as a powerful tool for the analysis of materials at the forefront in catalysis, nano-electronics, therapy or imaging. It should therefore strongly impact these fields in a near future.

The developments of new methodologies pave the way to routine electron tomography experiments with atomic resolution for the next years. Further improvements are yet still needed, and one first task will be to reduce the number of projections needed to obtain reliable results, using hardware implementation of compressive sensing approach, based on the fact that a reduced number of well-chosen recordings can suffice to reconstruct images or volumes given by sparse objects.[97] By diminishing the total irradiation dose during the acquisition, this approach will allow a considerable increase of the SNR in the acquired projections as well as the study of more fragile materials. Within the limitations related to damage of the sample upon electronic irradiation, they will also bring alive the possibility of combining high-quality 3D structural and chemical determination with measurements conducted in environmental TEM (eg. under a pressure of gas) or using *in situ* cells sample holder (eg. liquid cell)[173].

Acknowledgements

CNRS, Collège de France and UPMC are acknowledged for financial support. The authors acknowledge the French CNRS (Centre National de la Recherche Scientifique) (FR3507), CEA (Commissariat à l'Energie Atomique) and METSA (Microscopie Electronique et Sonde Atomique) network. Ovidiu Ersen acknowledges the Institut Universitaire de France (IUF). The Foundation of Collège de France and the support of Solvay are also aknowledged.

References

[1] G. Ozin, S. Arsenault, *Nanochemistry: A Chemical Approach to Nanomaterials*, RSC Publishing, **2005**.

[2] C. J. Brinker, G. W. Scherer, *Sol-Gel Science, The Physics and Chemistry of Sol-Gel Processing*, Academic Press, San Diego, **1990**.

[3] J. Livage, M. Henry, C. Sanchez, *Prog. Solid State Chem.* **1988**, *18*, 259–341.

[4] L. H. Reddy, J. L. Arias, J. Nicolas, P. Couvreur, *Chem. Rev.* **2012**, *112*, 5818–5878.

[5] M. C. Dos Santos, O. Kesler, A. L. M. Reddy, *J. Nanomater.* **2012**, *2012*, DOI 10.1155/2012/159249.

[6] S. Park, M. Vosguerichian, Z. Bao, *Nanoscale* **2013**, *5*, 1727–52.

[7] C. Sanchez, P. Belleville, M. Popall, L. Nicole, *Chem. Soc. Rev.* **2011**, *40*, 696–753.

[8] G. Schottner, *Chem. Mater.* **2001**, *13*, 3422–3435.

[9] O. Salata, *J. Nanobiotechnology* **2004**, *2*, 3.

[10] M. A. Aegerter, M. Mennig, **2004**.

[11] C. Sanchez, B. Julian, P. Belleville, M. Popall, *J. Mater. Chem.* **2005**, *15*, 3559–3592.

[12] H. Schmidt, *J. Sol-Gel Sci. Technol.* **2006**, *40*, 115–130.

[13] A. U. Czaja, N. Trukhan, U. Müller, *Chem. Soc. Rev.* **2009**, *38*, 1284–1293.

[14] J. Ramos, J. Forcada, R. Hidalgo-Alvarez, *Chem. Rev.* **2014**, *114*, 367–428.

[15] J. N. Freitas, A. S. Gonçalves, A. F. Nogueira, *Nanoscale* **2014**, *6*, 6371–97.

[16] L. Tosheva, V. P. Valtchev, *Chem. Mater.* **2005**, *17*, 2494–2513.

[17] S. Mann, S. L. Burkett, S. A. Davis, C. E. Fowler, N. H. Mendelson, S. D. Sims, D. Walsh, N. T. Whilton, *Chem. Mater.* **1997**, *9*, 2300–2310.

[18] G. A. Ozin, *Chem. Commun.* **2000**, *6*, 419–432.

[19] G. J. A. A. D. a a Soler-Illia, C. Sanchez, B. Lebeau, J. Patarin, *Chem. Rev.* **2002**, *102*, 4093–138.

[20] H. Colfen, M. Antonietti, *Angew. Chemie-International Ed.* **2005**, *44*, 5576–5591.

[21] F. C. Meldrum, H. Colfen, *Chem. Rev.* **2008**, *108*, 4332–4432.

[22] N. Brun, S. Ungureanu, H. Deleuze, R. Backov, *Chem. Soc. Rev.* **2011**, *40*, 771–788.

[23] C. Sanchez, H. Arribart, M. M. G. Guille, *Nat. Mater.* **2005**, *4*, 277–288.

[24] E. V Shevchenko, D. V Talapin, N. a Kotov, S. O'Brien, C. B. Murray, *Nature* **2006**, *439*, 55–59.

[25] M. Faustini, D. Grosso, C. Boissière, R. Backov, C. Sanchez, *J. Sol-Gel Sci. Technol.* **2014**, *70*, 216–226.

[26] J.-P. Jolivet, *Metal Oxide Chemistry and Synthesis: From Solution to Solid State*, Wiley, Chichester, **2000**.

[27] E. Matijević, P. Scheiner, *J. Colloid Interface Sci.* **1978**, *63*, 509–524.

[28] J. Turkevich, P. Stevenson, J. Hillier, *J. Phys. Chem.* **1953**, *57*, 670.

[29] D. S. Su, B. Zhang, R. Schlögl, *Chem. Rev.* **2015**, *115*, 150401095423003.

[30] H. Friedrich, P. E. De Jongh, A. J. Verkleij, K. P. De Jong, *Chem. Rev.* **2009**, *109*, 1613–1629.

[31] L. Carbone, P. D. Cozzoli, *Nano Today* **2010**, *5*, 449–493.

[32] R. Ferrando, J. Jellinek, R. L. Johnston, *Chem. Rev.* **2008**, *108*, 845–910.

[33] S. Zhou, M. Wen, N. Wang, Q. Q. Wu, Q. Q. Wu, L. Cheng, *J. Mater. Chem.* **2012**, *22*, 16858.

[34] B. W. Li, M. Osada, T. C. Ozawa, Y. Ebina, K. Akatsuka, R. Ma, H. Funakubo, T. Sasaki, *ACS Nano* **2010**, *4*, 6673–6680.

[35] F. Ocampo, B. Louis, A.-C. Roger, *Appl. Catal. A Gen.* **2009**, *369*, 90–96.

[36] K.-S. Cho, D. V Talapin, W. Gaschler, C. B. Murray, *J. Am. Chem. Soc.* **2005**, *127*, 7140–7.

[37] R. R. Zamani, M. Ibáez, M. Luysberg, N. García-Castelló, L. Houben, J. D. Prades, V. Grillo, R. E. Dunin-Borkowski, J. R. Morante, A. Cabot, et al., *ACS Nano* **2014**, *8*, 2290–2301.

[38] X. Gou, F. Cheng, Y. Shi, L. Zhang, S. Peng, J. Chen, P. Shen, *J. Am. Chem. Soc.* **2006**, *128*, 7222–9.

[39] Y. Chen, S. Hu, W. Liu, X. Chen, L. Wu, X. Wang, P. Liu, Z. Li, *Dalton Trans.* **2011**, *40*, 2607–13.

[40] W. Cai, Y. Zhao, J. Hu, J. Zhong, W. Xiang, *J. Mater. Sci. Technol.* **2011**, *27*, 559–562.

[41] S. Carenco, D. Portehault, C. Boissière, N. Mézailles, C. Sanchez, *Chem. Rev.* **2013**, *113*, 7981–8065.

[42] X. Ye, J. Chen, M. Engel, J. A. Millan, W. Li, L. Qi, G. Xing, J. E. Collins, C. R. Kagan, J. Li, et al., *Nat. Chem.* **2013**, *5*, 466–73.

[43] Y. Yan, J. Miao, Z. Yang, F.-X. Xiao, H. Bin Yang, B. Liu, Y. Yang, *Chem. Soc. Rev.* **2015**, DOI 10.1039/C4CS00492B.

[44] M. Xu, T. Liang, M. Shi, H. Chen, *Chem. Rev.* **2013**, *113*, 3766–3798.

[45] J. Nicolas, S. Mura, D. Brambilla, N. Mackiewicz, P. Couvreur, *Chem. Soc. Rev.* **2013**, *42*, 1147–235.

[46] S. Forster, M. Antonietti, *Adv. Mater.* **1998**, *10*, 195–+.

[47] E. Bourgeat-Lami, M. Lansalot, in *Hybrid Latex Part. Prep. With* (Eds.: A.M. VanHerk, K. Landfester), **2010**, pp. 53–123.

[48] O. Ersen, J. Werckmann, M. Houllé, M.-J. Ledoux, C. Pham-Huu, *Nano Lett.* **2007**, *7*, 1898–1907.

[49] M. Filippousi, S. Turner, M. Katsikini, F. Pinakidou, D. Zamboulis, E. Pavlidou, G. Van Tendeloo, *Microporous Mesoporous Mater.* **2015**, *210*, 185–193.

[50] S. Carenco, D. Portehault, C. Boissière, N. Mézailles, C. Sanchez, *Adv. Mater.* **2014**, *26*, 371–90.

[51] C. B. Murray, C. R. Kagan, M. G. Bawendi, *Annu. Rev. Mater. Res.* **2000**, *30*, 545–610.

[52] G. Möbus, B. J. Inkson, *Mater. Today* **2007**, *10*, 18–25.

[53] P. A. Midgley, E. P. W. Ward, A. B. Hungría, J. M. Thomas, *Chem. Soc. Rev.* **2007**, *36*, 1477–1494.

[54] O. Ersen, I. Florea, C. Hirlimann, *Mater. Today* **2015**, DOI 10.1016/j.mattod.2015.04.004.

[55] G. Van Tendeloo, S. Bals, S. Van Aert, J. Verbeeck, D. Van Dyck, *Adv. Mater.* **2012**, *24*, 5655–5675.

[56] L. Rodríguez-Lorenzo, R. de la Rica, R. A. Álvarez-Puebla, L. M. Liz-Marzán, M. M. Stevens, *Nat. Mater.* **2012**, *11*, 604–607.

[57] K. Miszta, J. de Graaf, G. Bertoni, D. Dorfs, R. Brescia, S. Marras, L. Ceseracciu, R. Cingolani, R. van Roij, M. Dijkstra, et al., *Nat. Mater.* **2011**, *10*, 872–876.

[58] J. Zhang, Y. Tang, L. Weng, M. Ouyang, *Nano Lett.* **2009**, *9*, 4061–4065.

[59] B. Sadtler, D. O. Demchenko, H. Zheng, S. M. Hughes, M. G. Merkle, U. Dahmen, L.-W. Wang, A. P. Alivisatos, *J. Am. Chem. Soc.* **2009**, *131*, 5285–5293.

[60] H. Jin Fan, M. Knez, R. Scholz, K. Nielsch, E. Pippel, D. Hesse, M. Zacharias, U. Gösele, *Nat. Mater.* **2006**, *5*, 627–631.

[61] R. Arenal, L. Henrard, L. Roiban, O. Ersen, J. Burgin, M. Treguer-Delapierre, *J. Phys. Chem. C* **2014**, *118*, 25643–25650.

[62] S. Jun, Sang Hoon Joo, R. Ryoo, M. Kruk, M. Jaroniec, Z. Liu, T. Ohsuna, O. Terasaki, *J. Am. Chem. Soc.* **2000**, *122*, 10712–10713.

[63] C. Sanchez, C. Boissiere, S. Cassaignon, C. Chaneac, O. Durupthy, M. Faustini, D. Grosso, C. Laberty-Robert, L. Nicole, D. Portehault, et al., *Chem. Mater.* **2014**, *26*, 221–238.

[64] M. Niederberger, *Acc. Chem. Res.* **2007**, *40*, 793–800.

[65] N. Pinna, M. Niederberger, *Angew. Chemie-International Ed.* **2008**, *47*, 5292–5304.

[66] P. H. Mutin, A. Vioux, *Chem. Mater.* **2009**, *21*, 582–596.

[67] S. Kitagawa, R. Kitaura, S. Noro, *Angew. Chemie-International Ed.* **2004**, *43*, 2334–2375.

[68] G. Ferey, C. Mellot-Draznieks, C. Serre, F. Millange, *Acc. Chem. Res.* **2005**, *38*, 217–225.

[69] J. Long, O. Yaghi, **2009**.

[70] A. Bétard, R. A. Fischer, *Chem. Rev.* **2012**, *112*, 1055–1083.

[71] P. Horcajada, R. Gref, T. Baati, P. K. Allan, G. Maurin, P. Couvreur, G. Ferey, R. E. Morris, C. Serre, *Chem. Rev.* **2012**, *112*, 1232–1268.

[72] D. Plana, J. Flórez-Montaño, V. Celorrio, E. Pastor, D. J. Fermín, *Chem. Commun. (Camb).* **2013**, *49*, 10962–4.

[73] E. Gonzalez, J. Arbiol, V. F. Puntes, *Science (80-.).* **2011**, *334*, 1377–1380.

[74] P. C. Lebaron, Z. Wang, T. J. Pinnavaia, *Appl. Clay Sci.* **1999**, *15*, 11–29.

[75] V. Nicolosi, M. Chhowalla, M. G. Kanatzidis, M. S. Strano, J. N. Coleman, *Science (80-.).* **2013**, *340*, 1226419.

[76] F. M. M. Fernandes, H. Baradari, C. Sanchez, D. Paris, *Appl. Clay Sci.* **2014**, *100*, 2–21.

[77] S. A. Claridge, A. W. Castleman, S. N. Khanna, C. B. Murray, A. Sen, P. S. Weiss, *ACS Nano* **2009**, *3*, 244–255.

[78] L. Rozes, C. Sanchez, *Chem. Soc. Rev.* **2011**, *40*, 1006–1030.

[79] J. Park, J. Joo, S. G. Kwon, Y. Jang, T. Hyeon, *Angew. Chem. Int. Ed. Engl.* **2007**, *46*, 4630–60.

[80] C. B. C. David. B. Williams, *Transmission Electron Microscopy, a Textbook for Materials Science, 2nd Edition*, Springer, New York, **2009**.

[81] D. Portehault, S. Cassaignon, E. Baudrin, J.-P. Jolivet, *J. Mater. Chem.* **2009**, *19*, 2407.

[82] D. Portehault, S. Cassaignon, E. Baudrin, J.-P. Jolivet, *Chem. Commun. (Camb).* **2009**, 674–6.

[83] D. Portehault, S. Cassaignon, E. Baudrin, J.-P. Jolivet, *Cryst. Growth Des.* **2009**, *9*, 2562–2565.

[84] D. Portehault, S. Cassaignon, E. Baudrin, J.-P. Jolivet, *J. Mater. Chem.* **2009**, *19*, 7947.

[85] D. Portehault, S. Cassaignon, E. Baudrin, J.-P. Jolivet, *J. Mater. Chem.* **2009**, *19*, 2407.

[86] T. Ishitani, T. Yaguchi, *Microsc. Res. Tech.* **1996**, *35*, 320–333.

[87] N. D. BASSIM, B. T. DE GREGORIO, A. L. D. KILCOYNE, K. SCOTT, T. CHOU, S. WIRICK, G. CODY, R. M. STROUD, *J. Microsc.* **2012**, *245*, 288–301.

[88] J. Radon, *Ben. Vehr. K. Sächs. Ges. Wiss. Leipzig Math-Phys. Kl.* **1917**, *69*, 262.

[89] R. G. Hart, *Science (80-.).* **1968**, *159*, 1464.

[90] D. J. De Rosier, A. Klug, *Nature* **1968**, *217*, 130.

[91] W. Hoppe, R. Langer, G. Knesch, C. Poppe, *Naturwissenschaften* **1968**, *55*, 333.

[92] A. M. Cormack, *J. Appl. Phys.* **1964**, *35*, 2908–2913.

[93] O. Medalia, I. Weber, A. S. Frangakis, D. Nicastro, G. Gerisch, W. Baumeister, *Science* **2002**, *298*, 1209–13.

[94] R. Gordon, R. Bender, G. T. Herman, *J. Theor. Biol.* **1970**, *29*, 471–481.

[95] P. Gilbert, *J. Theor. Biol.* **1972**, *36*, 105–117.

[96] K. J. Batenburg, S. Bals, J. Sijbers, C. Kübel, P. A. Midgley, J. C. Hernandez, U. Kaiser, E. R. Encina, E. A. Coronado, G. Van Tendeloo, *Ultramicroscopy* **2009**, *109*, 730–740.

[97] Z. Saghi, D. J. Holland, R. Leary, A. Falqui, G. Bertoni, A. J. Sederman, L. F. Gladden, P. A. Midgley, *Nano Lett.* **2011**, *11*, 4666–4673.

[98] M. C. Scott, C.-C. Chen, M. Mecklenburg, C. Zhu, R. Xu, P. Ercius, U. Dahmen, B. C. Regan, J. Miao, *Nature* **2012**, *483*, 444–447.

[99] C.-C. Chen, C. Zhu, E. R. White, C.-Y. Chiu, M. C. Scott, B. C. Regan, L. D. Marks, Y. Huang, J. Miao, *Nature* **2013**, *496*, 74–77.

[100] K. van Benthem, A. R. Lupini, M. Kim, H. S. Baik, S. Doh, J.-H. Lee, M. P. Oxley, S. D. Findlay, L. J. Allen, J. T. Luck, et al., *Appl. Phys. Lett.* **2005**, *87*, 034104.

[101] S. Van Aert, K. J. Batenburg, M. D. Rossell, R. Erni, G. Van Tendeloo, *Nature* **2011**, *470*, 374–377.

[102] B. Goris, J. De Beenhouwer, A. De Backer, D. Zanaga, K. J. Batenburg, A. Sánchez-Iglesias, L. M. Liz-Marzán, S. Van Aert, S. Bals, J. Sijbers, et al., *Nano Lett.* **2015**, *15*, 6996–7001.

[103] A. J. Koster, U. Ziese, A. J. Verkleij, A. H. Janssen, K. P. De Jong, *J. Phys. Chem. B* **2000**, *104*, 9368–9370.

[104] L. Roiban, L. Hartmann, A. Fiore, D. Djurado, F. Chandezon, P. Reiss, J.-F. Legrand, S. Doyle, M. Brinkmann, O. Ersen, *Nanoscale* **2012**, *4*, 7212.

[105] D. Georgescu, L. Roiban, O. Ersen, D. Ihiawakrim, L. Baia, S. Simon, *RSC Adv.* **2012**, *2*, 5358.

[106] P. A. Midgley, M. Weyland, *Ultramicroscopy* **2003**, *96*, 413–431.

[107] R. D. Leapman, E. Kocsis, G. Zhang, T. L. Talbot, P. Laquerriere, *Ultramicroscopy* **2004**, *100*, 115–125.

[108] P. A. Midgley, M. Weyland, in *Ultramicroscopy*, **2003**, pp. 413–431.

[109] L. Roiban, L. Sorbier, C. Pichon, P. Bayle-Guillemaud, J. Werckmann, M. Drillon, O. Ersen, *Microsc. Microanal.* **2012**, *18*, 1118–1128.

[110] G. Mȍbus, B. J. Inkson, *Appl. Phys. Lett.* **2001**, *79*, 1369.

[111] I. Florea, O. Ersen, C. Hirlimann, L. Roiban, A. Deneuve, M. Houllé, I. Janowska, P. Nguyen, C. Pham, C. Pham-Huu, *Nanoscale* **2010**, *2*, 2668.

[112] L. Roiban, L. Sorbier, C. Pichon, P. Bayle-Guillemaud, J. Werckmann, M. Drillon, O. Ersen, *Microsc. Microanal.* **2012**, *18*, 1118–1128.

[113] K. Lepinay, F. Lorut, R. Pantel, T. Epicier, *Micron* **2013**, *47*, 43–49.

[114] P. A. Midgley, C. Durkan, *Mater. Today* **2008**, *11*, 8–11.

[115] J. M. Rosenholm, C. Sahlgren, M. Lindén, *Nanoscale* **2010**, *2*, 1870–83.

[116] Y. Lin, K. R. Hurley, C. L. Haynes, *J. Phys. Chem. Lett.* **2012**, *3*, 364–374.

[117] R. Mortera, S. Fiorilli, E. Garrone, E. Verné, B. Onida, *Chem. Eng. J.* **2010**, *156*, 184–192.

[118] B. Julian-Lopez, C. Boissiere, C. Chaneac, D. Grosso, S. Vasseur, S. Miraux, E. Duguet, C. Sanchez, *J. Mater. Chem.* **2007**, *17*, 1563–1569.

[119] M. Colilla, M. Manzano, I. Izquierdo-Barba, M. Vallet-Regi, C. Boissiere, C. Sanchez, *Chem. Mater.* **2010**, *22*, 1821–1830.

[120] T. Fontecave, C. Sanchez, T. Azais, C. Boissiere, *Chem. Mater.* **2012**, *24*, 4326–4336.

[121] T. Fontecave, C. Boissiere, N. Baccile, F. J. Plou, C. Sanchez, *Chem. Mater.* **2013**, *25*, 4671–4678.

[122] C. Boissiere, D. Grosso, A. Chaumonnot, L. Nicole, C. Sanchez, *Adv. Mater.* **2010**, *23*, 599–623.

[123] F. Rambaud, K. Valle, S. Thibaud, B. Julian-Lopez, C. Sanchez, *Adv. Funct. Mater.* **2009**, *19*, 2896–2905.

[124] N. Stock, S. Biswas, *Chem. Rev.* **2012**, *112*, 933–69.

[125] G. Férey, *Chem. Soc. Rev.* **2008**, *37*, 191–214.

[126] J. L. C. Rowsell, O. M. Yaghi, *Microporous Mesoporous Mater.* **2004**, *73*, 3–14.

[127] O. Delgado-Friedrichs, M. D. Foster, M. O'Keeffe, D. M. Proserpio, M. M. J. Treacy, O. M. Yaghi, *J. Solid State Chem.* **2005**, *178*, 2533–2554.

[128] V. Stavila, A. A. Talin, M. D. Allendorf, *Chem. Soc. Rev.* **2014**, *43*, 5994–6010.

[129] Y. He, W. Zhou, G. Qian, B. Chen, *Chem. Soc. Rev.* **2014**, *43*, 5657–5678.

[130] A. Dhakshinamoorthy, M. Alvaro, H. Garcia, *Chem. Commun. (Camb).* **2012**, *48*, 11275–88.

[131] T. Zhang, W. Lin, *Chem. Soc. Rev.* **2014**, DOI 10.1039/c4cs00103f.

[132] Z. Zhang, Y. Zhao, Q. Gong, Z. Li, J. Li, *Chem. Commun.* **2013**, *49*, 653–661.

[133] M. P. Suh, H. J. Park, T. K. Prasad, D.-W. Lim, *Chem. Rev.* **2012**, *112*, 782–835.

[134] J. L. C. Rowsell, O. M. Yaghi, *Angew. Chem. Int. Ed. Engl.* **2005**, *44*, 4670–9.

[135] J. Park, J.-R. Li, Y.-P. Chen, J. Yu, A. A. Yakovenko, Z. U. Wang, L.-B. Sun, P. B. Balbuena, H.-C. Zhou, *Chem. Commun. (Camb).* **2012**, *48*, 9995–7.

[136] M. Dan-Hardi, C. Serre, T. Frot, L. Rozes, G. Maurin, C. Sanchez, G. Férey, *J. Am. Chem. Soc.* **2009**, *131*, 10857–9.

[137] A. Walsh, C. R. A. Catlow, *Chemphyschem* **2010**, *11*, 2341–4.

[138] S. M. Cohen, *Chem. Rev.* **2012**, *112*, 970–1000.

[139] P. Deria, J. E. Mondloch, O. Karagiaridi, W. Bury, J. T. Hupp, O. K. Farha, *Chem. Soc. Rev.* **2014**, 41–44.

[140] W. Lu, Z. Wei, Z.-Y. Gu, T.-F. Liu, J. Park, J. Park, J. Tian, M. Zhang, Q. Zhang, T. Gentle Iii, et al., *Chem. Soc. Rev.* **2014**, *43*, 5561.

[141] Y. Fu, D. Sun, Y. Chen, R. Huang, Z. Ding, X. Fu, Z. Li, *Angew. Chem. Int. Ed. Engl.* **2012**, *51*, 3364–7.

[142] Y. Horiuchi, T. Toyao, M. Saito, K. Mochizuki, M. Iwata, H. Higashimura, M. Anpo, M. Matsuoka, *J. Phys. Chem. C* **2012**, *116*, 20848–20853.

[143] S.-N. Kim, J. Kim, H.-Y. Kim, H.-Y. Cho, W.-S. Ahn, *Catal. Today* **2013**, *204*, 85–93.

[144] C. H. Hendon, D. Tiana, M. Fontecave, C. Sanchez, L. D'arras, C. Sassoye, L. Rozes, C. Mellot-Draznieks, A. Walsh, *J. Am. Chem. Soc.* **2013**, *135*, 10942–5.

[145] M. Chambers, X. Wang, C. Hendon, C. Sanchez, M. Fontecave, L. Rozes, C. Mellot-Draznieks, **n.d.**, in preparation.

[146] H. G. Von Schnering, W. Hoenle, *Chem. Rev.* **1988**, *88*, 243–273.

[147] S. Carenco, D. Portehault, C. Boissière, N. Mézailles, C. Sanchez, *Chem. Rev.* **2013**, *113*, 7981–8065.

[148] S. T. Oyama, T. Gott, H. Zhao, Y.-K. Lee, *Catal. Today* **2009**, *143*, 94–107.

[149] E. Bekaert, J. Bernardi, S. Boyanov, L. Monconduit, M.-L. Doublet, M. Ménétrier, *J. Phys. Chem. C* **2008**, *112*, 20481–20490.

[150] A. Nelson, M. Sun, A. Junaid, *J. Catal.* **2006**, *241*, 180–188.

[151] S. Carenco, A. Leyva-Pérez, P. Concepción, C. Boissière, N. Mézailles, C. Sanchez, A. Corma, *Nano Today* **2012**, *7*, 21–28.

[152] S. Carenco, C.-H. Wu, A. Shavorskiy, S. Alayoglu, G. A. Somorjai, H. Bluhm, M. Salmeron, *Small* **2015**, DOI 10.1002/smll.201402795.

[153] S. Carenco, I. Resa, X. Le Goff, P. Le Floch, N. Mézailles, *Chem. Commun.* **2008**, 2568–70.

[154] S. Carenco, M. Demange, J. Shi, C. Boissière, C. Sanchez, P. Le Floch, N. Mézailles, C. Boissiere, N. Mezailles, *Chem. Commun.* **2010**, *46*, 5578–80.

[155] S. Carenco, Y. Hu, I. Florea, O. Ersen, C. Boissière, N. Mézailles, C. Sanchez, *Chem. Mater.* **2012**, *24*, 4134–4145.

[156] S. Carenco, D. Portehault, C. Boissière, N. Mézailles, C. Sanchez, *Adv. Mater.* **2014**, *26*, 371–389.

[157] S. Carenco, Y. Hu, I. Florea, O. Ersen, C. Boissière, C. Sanchez, N. Mézailles, *Dalt. Trans.* **2013**, *42*, 12667–12674.

[158] S. Carenco, I. Florea, O. Ersen, C. Boissière, N. Mézailles, C. Sanchez, *New J. Chem.* **2013**, *37*, 1231–1237.

[159] S. Carenco, C. Boissière, L. Nicole, C. Sanchez, P. Le Floch, N. Mézailles, *Chem. Mater.* **2010**, *22*, 1340–1349.

[160] S. Carenco, X. F. Le Goff, J. Shi, L. Roiban, O. Ersen, C. Boissière, C. Sanchez, N. Mézailles, *Chem. Mater.* **2011**, *23*, 2270–2277.

[161] P. A. Midgley, M. Weyland, T. Yates, J. Tong, R. E. Dunin-Borkowski, J. M. Thomas, *Microsc. Microanal.* **2004**, *10*, 148–149.

[162] K. Jarausch, P. Thomas, D. N. Leonard, R. Twesten, C. R. Booth, *Ultramicroscopy* **2009**, *109*, 326–337.

[163] M. A. Aronova, Y. C. Kim, G. Zhang, R. D. Leapman, *Ultramicroscopy* **2007**, *107*, 232–244.

[164] M. A. Aronova, Y. C. Kim, R. Harmon, A. A. Sousa, G. Zhang, R. D. Leapman, *J. Struct. Biol.* **2008**, *161*, 322–335.

[165] C. S. Bonifacio, S. Carenco, C. H. Wu, S. D. House, H. Bluhm, J. C. Yang, *Chem. Mater.* **2015**, 151007114828001.

[166] B. K. Miller, P. A. Crozier, *Microsc. Microanal.* **2013**, *19*, 461–469.

[167] X. Chen, C. Li, H. Cao, *Nanoscale* **2015**, *7*, 4811–4819.

[168] S. Zhao, Y. Li, E. Stavitski, R. Tappero, S. Crowley, M. J. Castaldi, D. N. Zakharov, R. G. Nuzzo, A. I. Frenkel, E. A. Stach, *ChemCatChem* **2015**, n/a–n/a.

[169] T. Xu, L. Sun, *Small* **2015**, *11*, 3247–3262.

[170] T. Schuh, N. de Jonge, *Comptes Rendus Phys.* **2014**, *15*, 214–223.

[171] G. Zhu, Y. Jiang, W. Huang, H. Zhang, F. Lin, C. Jin, *Chem. Commun.* **2013**, *49*, 10944.

[172] H.-G. Liao, H. Zheng, *J. Am. Chem. Soc.* **2013**, *135*, 5038–5043.

[173] Q. Chen, H. Cho, K. Manthiram, M. Yoshida, X. Ye, A. P. Alivisatos, *ACS Cent. Sci.* **2015**, *1*, 33–39.